HHS Public Access

Author manuscript

Cell Rep. Author manuscript; available in PMC 2023 September 27.

Published in final edited form as:

Cell Rep. 2023 July 25; 42(7): 112706. doi:10.1016/j.celrep.2023.112706.

Autism-linked UBE3A gain-of-function mutation causes interneuron and behavioral phenotypes when inherited maternally or paternally in mice

Lei Xing[1], **Jeremy M. Simon**[1,3,4], **Travis S. Ptacek**[1,3], **Jason J. Yi**[1,2,3,5], **Lipin Loo**[1,2], **Hanqian Mao**[1,2,3], **Justin M. Wolter**[1,2,3,4], **Eric S. McCoy**[1,2], **Smita R. Paranjape**[1,2], **Bonnie Taylor-Blake**[1,2], **Mark J. Zylka**[1,2,3,6,*]

[1]UNC Neuroscience Center, The University of North Carolina at Chapel Hill, Chapel Hill, NC 27599, USA

[2]Department of Cell Biology and Physiology, The University of North Carolina at Chapel Hill, Chapel Hill, NC 27599, USA

[3]Carolina Institute for Developmental Disabilities, The University of North Carolina at Chapel Hill, Campus Box #7255, Chapel Hill, NC 27599, USA

[4]Department of Genetics, The University of North Carolina at Chapel Hill, Campus Box #7264, Chapel Hill, NC 27599, USA

[5]Present address: Department of Neuroscience, Washington University School of Medicine, St. Louis, MO 63110, USA

[6]Lead contact

SUMMARY

The E3 ubiquitin ligase *Ube3a* is biallelically expressed in neural progenitors and glial cells, suggesting that UBE3A gain-of-function mutations might cause neurodevelopmental disorders irrespective of parent of origin. Here, we engineered a mouse line that harbors an autism-linked UBE3A^{T485A} (T503A in mouse) gain-of-function mutation and evaluated phenotypes in animals that inherited the mutant allele paternally, maternally, or from both parents. We find that paternally and maternally expressed UBE3A^{T503A} results in elevated UBE3A activity in neural progenitors and glial cells. Expression of UBE3A^{T503A} from the maternal allele, but not the paternal one, leads to a persistent elevation of UBE3A activity in neurons. Mutant mice display behavioral phenotypes that differ by parent of origin. Expression of UBE3A^{T503A}, irrespective of its parent

*Correspondence: zylka@med.unc.edu.

AUTHOR CONTRIBUTIONS

L.X., J.M.S., and M.J.Z. designed the study. L.X., J.M.S., T.S.P., L.L., J.J.Y., H.M., J.M.W., E.S.M., S.R.P., and B.T.-B. conducted the experiments and analyzed the data. M.J.Z. supervised the project. L.X., J.M.S., and M.J.Z. wrote the manuscript, and all authors provided feedback and approved the final manuscript.

DECLARATION OF INTERESTS

The authors declare no competing interests.

SUPPLEMENTAL INFORMATION

Supplemental information can be found online at https://doi.org/10.1016/j.celrep.2023.112706.

of origin, promotes transient embryonic expansion of *Zcchc12* lineage interneurons. Phenotypes of *Ube3a*^{T503A} mice are distinct from Angelman syndrome model mice. Our study has clinical implications for a growing number of disease-linked UBE3A gain-of-function mutations.

In brief

Xing et al. describe a mouse line modeling an autism-linked UBE3A gain-of-function point mutation. The authors show that UBE3A gain of function results in neurodevelopmental phenotypes distinct from Angelman syndrome model mice and how these phenotypes are influenced by parental inheritance.

Graphical Abstract

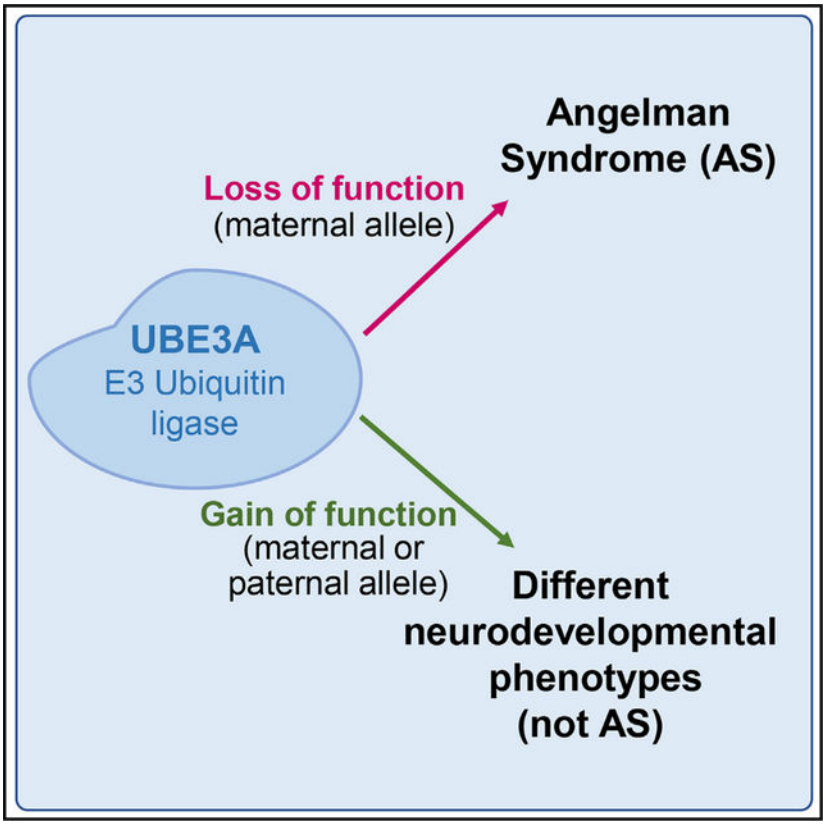

INTRODUCTION

UBE3A is a HECT domain-containing E3 ubiquitin ligase that targets substrate proteins, including itself, for proteasome-mediated degradation.[1] Aberrant UBE3A activity and function is linked to neurodevelopmental disorders and cervical cancer.[2,3] UBE3A is biallelically expressed in mitotic cells, including neural progenitors and non-neuronal cells. However, the paternally inherited allele is gradually silenced as neurons mature, resulting in expression of UBE3A primarily from the maternal allele in postmitotic neurons.[4] Deletion or mutation of the maternal allele resulting in UBE3A loss of function causes Angelman syndrome (AS), a severe neurodevelopmental disorder with symptoms

that include intellectual disability, microcephaly, seizures, a happy demeanor, speech impairment, and motor dysfunction.[3,5–7] Duplication or triplication of maternal *UBE3A* is linked to neurodevelopmental disorders with clinical features that are distinct from AS.[6,8–10] Overall, these disorders highlight how precise regulation of *UBE3A* expression and function is necessary for normal brain development.

As part of a large exome sequencing study, Iossifov et al. identified a male autism proband with a threonine 485 to alanine (T485A) missense mutation in UBE3A.[11] Subsequently, we found that this autism-linked UBE3A^{T485A} missense mutation elevated UBE3A ubiquitin ligase activity, indicative of gain of function.[12] When overexpressed in HEK293 cells, UBE3A^{T485A} hyperubiquitinated and promoted the degradation of UBE3A and PSMD4,[12,13] a proteasome subunit that directly interacts with UBE3A.[14–16] Additionally, we found that UBE3A and two endogenous substrates were reduced at the protein level in an immortalized lymphocyte cell line derived from the UBE3A^{T485A} autism proband relative to cells from the parents, both carrying wildtype UBE3A alleles.[12] However, whether this gain-of-function mutation was expressed from the maternally or paternally inherited chromosome in the autism proband was not known.

Additional gain-of-function missense mutations in UBE3A were subsequently identified, and 17 individuals with these mutations were clinically characterized and found to have symptoms that differed from AS.[17] Among these affected individuals, 7 individuals carried gain-of-function mutations that were maternally inherited, and one showed paternal inheritance, while the parent of origin for the rest was not established.[17] These data suggest that maternal or paternal transmission of UBE3A gain-of-function mutations might cause neurodevelopmental disorders. UBE3A is biallelically expressed in neural progenitors and other mitotic cell types,[4] so it is possible that UBE3A gain-of-function mutations could impact brain development or non-neuronal cells in ways that differ from UBE3A loss of function. Here, we sought to evaluate whether UBE3A gain of function and parent of origin influence brain development and neurodevelopmental phenotypes, with a focus on UBE3A^{T485A}, the first UBE3A gain-of-function mutation linked to a neurodevelopmental disorder.

RESULTS

Autism proband *UBE3A^{T485A}* mutation is on the paternal chromosome

To determine if the *UBE3A^{T485A}* missense mutation was on the maternally or paternally inherited chromosome in the autism proband,[11,12] we used 10× Genomics linked-read sequencing to haplotype phase the mutation relative to exonic single-nucleotide polymorphisms (SNPs). This entailed whole-genome sequencing of the lymphoblastoid cell line from the proband at >23× coverage and comparing this phased genome with published exome sequencing data from the unaffected parents.[11] This analysis revealed that the de *novo* mutation (T>C; T485A based on Genebank: NP_570853.1, human isoform 1; T505A based on Genebank: NP_570854.1, human isoform 3; T508A based on Genebank: NP_000453.2, human isoform 2) co-segregates with paternally inherited SNPs (haplotype 1, Figure 1; reference genomic assembly: hgGRCh37/hg19), placing the T485A mutation on the paternally inherited chromosome.

Subsequent to describing this autism-linked *UBE3A*^{T485A} mutation,[12] we were contacted by a clinician who identified a child with autism and intellectual disability with a maternally inherited *UBE3A*^{T787A} mutation (ClinVar variant ID 418562; T787A based on Genebank: NP_570853.1; T807A based on Genebank: NP_570854.1; T810A based on Genebank: NP_000453.2). This affected individual was also described in Weston et al. along with a sibling who inherited the *UBE3A*^{T787A} mutation maternally.[17]

To determine if this UBE3A^{T787A} variant altered UBE3A activity, we overexpressed MYC-tagged UBE3A^{WT}, UBE3A^{T787A}, UBE3A^{T485A}, and their corresponding ligase-dead (LD; C820A) versions in HEK293 cells and examined levels of MYC-UBE3A and PSMD4 by western blot (Figures S1A and S1B). The UBE3A^{T787A} variant significantly reduced the protein levels of MYC-UBE3A and PSMD4 in a ligase-dependent manner, like MYC-UBE3A^{T485A} (Figure S1B), consistent with gain of function.

We previously used a WNT/β-catenin reporter assay to distinguish UBE3A loss-of-function from gain-of-function mutations.[13] Using this assay, we found that UBE3A^{T787A} stimulated WNT/β-catenin reporter gene activation to a greater extent than UBE3A^{WT} and that such activation was ubiquitin ligase dependent (Figure S1C), consistent with UBE3A gain of function. Similar results were independently replicated by Weston et al.[17]

Generation of *Ube3a*^{T503A} mouse that models the human *UBE3A*^{T485A} mutation

While clinical data suggest that neurodevelopmental deficits can arise when UBE3A gain-of-function mutations are inherited maternally or paternally,[17] the number of affected individuals, particularly those showing paternal inheritance, is small, and penetrance in humans, based on the limited clinical data currently available, appears to be variable. To permit rigorous control over parent of origin and genetic background, we utilized CRISPR-Cas9 homology-directed recombination to engineer a mouse that models the human *UBE3A*^{T485A} mutation at the synonymous T503 residue on a pure C57BL/6J background. We introduced an ACT>GCA mutation in exon 6 of the mouse *Ube3a* gene, which changes T503 to alanine (T503A; based on Genebank: NP_001380595.1, mouse isoform 2, equivalent to human isoform 3; T482A based on Genebank: NP_001029134.1, mouse isoform 3, equivalent to human isoform 1) (Figure 2A). A silent mutation was introduced near T503A to create an *AluI* site for genotyping. We verified that all introduced mutations were present by PCR and Sanger sequencing (Figure 2B). Wild-type (WT), heterozygous, and homozygous mutant mice can be distinguished by digesting the PCR fragment with *AluI* (Figure 2C). Mutant mice of all three genotypes were born at a normal Mendelian ratio. We henceforth refer to these animals as *Ube3a*^{T503A} mutant mice and designate allele inheritance as maternal (matT503A), paternal (patT503A), or both maternal and paternal (homoT503A).

In vivo UBE3A^{T503A} gain-of-function activity differs from UBE3A loss of function

We first determined if levels of UBE3A and its interacting proteins were altered in the brain of *Ube3a*^{T503A} mutant mice. We and Weston et al. previously found that UBE3A gain of function results in hyperubiquitination of UBE3A substrates, including UBE3A itself, with its molecular consequence substantiated as a reduction in protein levels.[12,13,17] We

found that UBE3A protein levels in the cortex were significantly reduced at embryonic day (E)14.5 in all three mutant genotypes compared with WT controls (Figure 2D), consistent with biallelic expression of *Ube3a* at embryonic ages.[4] UBE3A levels were also significantly reduced in the cerebral cortex of all three genotypes at postnatal day 0 (P0), although UBE3A levels approached WT levels in patT503A mice (Figure 2E). In adult animals, UBE3A protein levels were significantly reduced only in matT503A and homoT503A mice (Figures 2F, S2A, and S2B), consistent with gradual extinction of paternal *Ube3a* expression in postmitotic neurons.[4]

Levels of three additional proteins were significantly reduced in samples from adult homoT503A mice (Figure 2G), including PSMD4, PSMD1, and NEURL4. All three proteins are in close proximity to UBE3A via direct or indirect protein interactions. PSMD4 directly interacts with UBE3A[14,16] and is a substrate of UBE3A in *Drosophila*,[18] the ubiquitination of PSMD1 is enhanced by UBE3A overexpression,[13] and NEURL4 associates with UBE3A through HERC2/NEURL4/ERK3 complexes.[19] A significant reduction in protein levels of PSMD4 and NEURL4 was also detected in matT503A mice (Figure S2A), but not in patT503A mice (Figure S2B). However, we did not detect differences in RAD23A (Figures 2F, S2A, and S2B), a previously identified substrate of UBE3A[20,21] that was reduced in lymphocytederived cell lines from the proband carrying the paternal *UBE3A*^{T485A} mutation.[12] While UBE3A protein levels are likewise reduced in the cerebral cortex of AS model (*Ube3a*$^{m-/p+}$) mice (Figure 2H), protein levels of PSMD4 were significantly increased in AS mice compared with WT controls, which contrasts with the reduction of PSMD4 in homoT503A mice (Figure 2G). Overall, these results indicate that gain and loss of function of UBE3A, while having similar effects on UBE3A protein levels, have opposite effects on PSMD4 levels *in vivo.*

We next examined UBE3A levels in brain cells by immunofluorescence staining. UBE3A protein levels were significantly reduced in progenitor cells (PAX6^{+}) in the ventricular zone (VZ) and sub-VZ (SVZ) of P0 brain sections from all three mutant genotypes (Figures 3A and 3B). UBE3A protein levels were also reduced in the neuronal layers of matT503A and homoT503A P0 mice but not in patT503A mice (Figures 3A and 3C). UBE3A protein levels were drastically reduced in cortical neurons in adult matT503A and homoT503A mice, but not in patT503A mice, compared with WT controls (Figures 3D and 3E). The relative subcellular abundance of UBE3A in cortical neurons was also altered in matT503A and homoT503A mice, showing a significant increase in the cytoplasm relative to the nucleus, compared with WT and patT503A mice (Figure 3F). In contrast, UBE3A protein levels were reduced to a similar extent in oligodendrocytes, a cell type that biallelically expresses *Ube3a*,[4] in all three mutant genotypes compared with controls (Figures 3G and 3H).

PSMD4 levels were also lower in homoT503A mouse neurons (Figures S3A and S3B). The interaction of PSMD4 and UBE3A was implicated in the nuclear localization of UBE3A.[15] While the proportion of nuclear UBE3A was reduced in cortical neurons of homoT503A mice (Figure 3F), the proportion of nuclear-localized PSMD4 was unchanged (Figure S3C). Collectively, these data indicate that the UBE3A^{T503A} mutation exerts gain-of-function activity in the developing and adult brain regardless of parent of origin, permitting us to

utilize *Ube3a*^{T503A} mice to investigate allele-specific effects of UBE3A gain-of-function in animals.

UBE3A^{T503A} does not grossly affect brain size or cerebral cortex structure

Microcephaly is observed in individuals affected by AS[2,22] and in an AS mouse model,[23–25] so we sought to evaluate whether UBE3A gain of function had global effects on brain size or structure. Multiple litters were evaluated to control for variability between litters.[26] We found that matT503A, patT503A, homoT503A, and WT littermate controls had comparable brain and body weight at birth (Figures 4A–4C) and at 3 months of age (Figures 4F and 4G). All mutant mice showed normal cortical thickness and neuron placement at P0 (Figures 4D and 4E) and at 3 months of age (Figures 4H and 4I) and comparable numbers of cortical excitatory neurons when compared wth WT controls (Figure 4J).

Transcriptional profiling of the embryonic and adult cerebral cortex

We next evaluated the extent to which the *Ube3a*^{T503A} mutation affected gene expression in the cerebral cortex at one embryonic (E14.5) and three postnatal ages (1, 6, and 12 months). Transcriptional profiling was performed on male mice only. We collected tissue from all three mutant genotypes and WT controls and processed all samples in parallel to minimize batch effects. We identified a total of 4,928 differentially expressed genes (DEGs) across all 12 groups (3 mutant genotypes relative to WT × 4 time points) (Table S3). Principal-component analyses showed that genes differentially expressed are heavily affected by developmental stages (Figure S4), suggesting that some genes may be co-regulated over time. To test this hypothesis, we hierarchically clustered standardized log2 fold change values of all 4,928 transcripts relative to controls as a function of age (Table S3). Nine gene clusters were identified, each showing unique temporal changes relative to WT controls (Figures 5A and 5B; Table S4). We then performed Gene Ontology analysis to identify pathways or functional or structural components that are enriched in each cluster (Figure 5C; Table S5).

Clusters 1 and 3 contained the largest number of DEGs (944 and 1,624, respectively) (Figure 5A; Table S4). Genes in cluster 1 were transiently upregulated at E14.5 in all three mutant genotypes but remained largely unchanged relative to WT animals at postnatal ages (Figures 5A and 5B; Table S4). Genes related to neuronal development and functions were highly enriched in this cluster (Figure 5C; Table S5) and included interneuron markers, such as *Vip* and *Pvalb* (Figure 5A). Expression of genes in cluster 3 was unchanged at E14.5 but was upregulated at 1 month and gradually returned to WT levels at later time points (Figures 5A and 5B; Table S4). Genes related to the ribosome, mitochondrial part, metabolic process, oxidative phosphorylation, and Parkinson's disease were enriched in this cluster (Figure 5C; Table S5). Overall, we found that gene expression changes in all three mutant genotypes were similar across ages.

Single-cell transcriptomic analysis of developing mouse neocortex

To further examine how the *Ube3a*^{T503A} mutation affected embryonic brain development, we performed single-cell RNA sequencing (RNA-seq; Drop-seq) on the E14.5 and P0 cerebral cortex of homoT503A and WT mice, including male and female mice. These

single-cell data were collected in parallel to minimize batch effects and to permit direct comparisons, but the WT data were previously used to evaluate normative murine cortical development at the single-cell level.[27] E14.5 represents the midpoint of cortical development, where layers 4 and 5 are being formed and developing interneurons are populating. And by P0, neurons from all six cortical layers are born. A total of 22,190 single cells were analyzed (homoT503A: 7,612 and 4,370 cells at E14.5 and P0, respectively; WT: 7,359 and 2,849 cells at E14.5 and P0, respectively). Overall, we identified 40 cell clusters well defined by their unique gene expression signatures (Figure S5A), including excitatory neurons representing different cortical layers, VZ/SVZ progenitors and radial glia, interneurons, astrocytes, oligodendrocytes, microglia, endothelial cells, and choroid/ependymal cells, as well as non-cortical cells from neighboring brain structures (ganglionic eminences, striatum, thalamus), consistent with our prior study.[27] We quantified the proportions of cells in each cluster from WT and homoT503A mice at both ages. We observed a statistically significant difference in just one cell population: Int2 (cluster #5, highlighted by a red box), which was expanded in the homoT503A cortex at E14.5 (Figure S5B; 3.5% of WT cells, 6% of T485A cells; false discovery rate [FDR] = 0.0497).

Given that a subset of interneurons were increased in *Ube3a*^{T503A} mice, we next explored the lineage relationship between interneuron subtypes and ganglionic eminence (GE) progenitors; the latter give rise to cortical interneurons.[28] We performed a pseudotime analysis with all five interneuron clusters (Int1, Int2, Int2_Zic^{+}, Int3, and Int4) and all four mitotic cell clusters (#8, #24, #29, and #33) that expressed GE progenitor cell markers (*Mki63*$^{+}$/*Dlx1*$^{+}$/*Dlx2*$^{+}$) (Figure S5A). To increase the power of this analysis, we combined cells from both homoT503A and WT mice at E14.5 and P0. Our analysis revealed that GE progenitor cells are upstream and hence represent common precursors for all interneuron clusters (Figure 6A). Intriguingly, the developmental trajectory was bifurcated into two distinct interneuron lineages, with Int4 cells representing a possible intermediate. Lineage 1 was made up of Int2 and Int2_Zic^{+} cells and was distinct from lineage 2, made up of Int1 and Int3 cells (Figure 6A).

Since the Int2 interneurons exhibited a significant increase in proportion from the homoT503A cortex, we identified genes whose expression patterns varied across pseudotime in lineage 1. We found that Int2 and Int2_Zic^{+} were highly similar interneurons subtypes, both expressing high levels of *Zcchc12* (Figures 6B and S5A), a Zn^{2+} binding domain-containing transcription factor associated with X-linked mental retardation.[29,30] Int2_Zic^{+} cells also expressed relatively high levels of *Zic1* (Figures 6B and S5A), a protein critical for forebrain development.[31] The proportion of both of these two cell types was similar between WT and homoT503A mice by P0 (Figure S5B).

We performed hybridization chain reaction (HCR) using probes for *Zcchc12* and *Gad2*, a pan-interneuron marker, to validate the embryonic increase of Int2 cells. All three mutant genotypes were included to explore the effect of *Ube3a*^{T503A} parent of origin. At E14.5, the proportion of *Gad2*$^{+}$ cells that expressed high levels of *Zcchc12* transcripts (*Gad2*$^{+}$/*Zcchc12*$^{+}$ cells, Figure 6C) relative to the total *Gad2*$^{+}$ cells was significantly increased in all three mutant groups compared with control (Figure 6D). However, the *Gad2*$^{+}$/*Zcchc12*$^{+}$ cell population was comparable to control mice at P0 in all three genotypes (Figure 6E),

consistent with our single-cell RNA-seq (scRNA-seq) data (Figure S5B). To ascertain which postnatal interneuron subtypes express *Zcchc12*, and hence potentially originate from embryonic *Gad2*$^{+}$/*Zcchc12*$^{+}$ cells, we performed HCR experiments on P24 cortical sections from WT mice with probes for *Zcchc12, Gad2*, and one of the three classic interneuron markers, *Calb2, Sst*, or *Pvalb*.[32] We found that *Gad2*$^{+}$/*Zcchc12*$^{+}$ cells were frequently co-labeled with *Calb2* (Figure 6F) or Sst (Figure 6G), but none were labeled with *Pvalb* (Figure 6H). These data suggest that embryonic *Gad2*$^{+}$/*Zcchc12*$^{+}$ cells later mature into a subclass of *Calb2*- and/or Sst-expressing interneurons. Overall, our results suggest that UBE3A^{T503A} gain of function affects the development of a subset of cortical interneurons, irrespective of T503A allele parent of origin.

Behavioral phenotypes differ based on *Ube3a*^{T503A} allele parent of origin

Ube3a^{T503A} parent of origin has the potential to influence the severity and spectrum of behavioral phenotypes. Thus, we performed a battery of behavior tests to test this possibility. We collected three cohorts of adult mice, each containing WT mice and one mutant class (matT503A, patT503A, homoT503A). Overall, as summarized in Figure 7A, behavioral phenotypes were observed in all three genotypes (Figures 7 and S6), but the constellation of phenotypes differed by genotype, suggesting that the T503A gain-of-function allele influences behavior in a parent-of-origin-dependent manner.

Hyperactivity in homoT503A and matT503A mice in the open-field test—Open-field tests were performed at 18 weeks of age. HomoT503A and matT503A mice showed a significant increase in total distance traveled compared with WT controls (Figures 7B and 7C), suggesting that these mice were hyperactive. In contrast, center time and time spent rearing were not affected in matT503A or homoT503A mice (Figures 7E, 7F, 7H, and 7I). There was no significant difference between WT and patT503A mice in any open-field measure (Figures 7D, 7G, and 7J).

As age influences phenotypes in autism model mice,[33] open-field tests were performed again at 30–32, 43–44, and 50 weeks of age (Figures 7B–7J and S6). A significant increase in distance traveled was again observed at one or more additional ages in matT503A and homoT503A mice (Figures 7B, 7C, S6A–S6A‴, and S6B–S6B‴) but not in patT503A mice (Figures 7D and 6C–6C‴). Time spent in the center of the open-field arena was significantly increased in 50-week-old homoT503A and matT503A mice (Figures 7E, 7F, S6D–S6D‴, and S6E–S6E‴) but not in paternal mutant mice (Figures 7G and S6F–S6F‴). A significant increase in rearing time was observed at two ages in homoT503A mice (Figures 7H and S6G–S6G‴) but not in matT503A (Figures 7I and S6H–S6H‴) or patT503A (Figures 7J and S6I–S6I‴) mice.

Enhanced performance of matT503A mutant mice in the rotarod test—Accelerating rotarod tests were performed to evaluate potential changes in motor coordination and motor learning. Overall, no effect of genotype was detected for mutant mice of all three genotypes (Figures 7K–7M), except that enhanced performance was observed in matT503A mice in trial 4 (Figure 7L). Gradual increases in times on the rotarod were observed for all three mutant genotypes similar to the control mice during the

first three consecutive trials, suggesting that the *Ube3a*^{T503A} allele does not impair motor learning (Figures 7K–M). However, using a 300 s cutoff, which is commonly used,[34–36] may have prevented us from detecting a statistically significant enhancement on the rotarod test in more trials. Of note, a larger portion of trials with homoT503A mice reached the cutoff time relative to WT mice (mutant:WT; total, 14:3; trials 1–5: 0:0, 3:0, 5:1, 3:1, 3:1) (Figure 7K), and the same was true for matT503A mice (mutant:WT; total, 15:3; trials 1–5: 0:0, 0:0, 5:0, 4:0, 6:3) (Figure 7L), compared with patT503A mice (mutant:WT; total, 4:2; trials 1–5: 0:0, 0:1, 2:1: 0:0, 2:0) (Figure 7M).

Deficits in patT485A mutant mice in a three-chamber social test—A three-chamber social test was performed to evaluate whether the *Ube3a*^{T503A} mutation affects social interactions. HomoT503A (Figure 7N) and matT503A (Figure 7P) mice showed a strong preference for a caged novel mouse (social stimulus, stranger #1) over an empty cage (Empty) and performed equivalently to WT mice (Figures 7N and 7P). However, patT503A mutant mice failed to show a preference for stranger #1 over an empty cage (Figure 7R), indicative of a social deficit. All three genotypes showed a strong preference for a novel caged social stimulus (stranger #2) over a now-familiar animal (stranger #1), similar to WT mice (Figures 7O, 7Q, and 7S). Consistent with the hyperactivity phenotypes observed in open-field tests, homoT503A (Figures 7T and 7U) and matT503A (Figure 7W) mutant mice, but not patT503A mutant mice (Figures 7X and 7V), showed a significant increase in entry times compared with WT mice in one or both sessions of the tests. The presence of social stimuli (strangers #1 and #2) did not affect chamber preference for homoT503A and matT503A mice (Figures 7N, 7O, and 7Q), suggesting that the increase in entry times (Figure 7T, 7U, and 7W) was caused by a general elevation of exploratory activities as seen in open-field tests. Entry times for patT503A mice were not different from WT mice (Figures 7X and 7Y). Overall, these results demonstrate that UBE3A^{T503A} parent of origin differently affects mouse open-field and social behaviors.

DISCUSSION

Ube3a^{T503A} mice were engineered to permit rigorous control over genetic background and allele parent of origin. These mice had a spectrum of brain developmental, transcriptional, and behavioral phenotypes when the *Ube3a*^{T503A} allele was inherited maternally or paternally. And as expanded upon below, these phenotypes differed from mice that model AS, a syndromic *UBE3A* loss-of-function neurodevelopmental disorder (Table S2). Our findings are consistent with emerging clinical findings. Weston et al. identified additional gain-of-function UBE3A mutations that associate with neurodevelopmental symptoms in humans,[17] including the UBE3A^{T787A} point mutation that we independently characterized above. Most of these UBE3A gain-of-function mutations were maternally inherited or are of undetermined inheritance. Like the autism-linked UBE3A^{T485A} mutation, paternal transmission was observed in one individual with intellectual disability and motor delays (individual 12).[17] Thus, UBE3A gain-of-function mutations appear to cause neurodevelopmental disorders in humans irrespective of parent of origin, with symptoms that differ from AS.

Our work provides insights into why UBE3A gain-of-function mutations cause phenotypes, and presumably disease, in humans when inherited maternally or paternally. Much focus has been paid to maternal-only expression of UBE3A in mature neurons. However, UBE3A is expressed biallelically throughout the body in mitotic cells,[4] including neural progenitors, astrocytes, and oligodendrocytes. Unlike loss-of-function mutations, gain-of-function mutations can dominantly interfere with the function of the WT protein. Indeed, we found that UBE3A protein levels were reduced below 50% in the brain of heterozygous matT503A mice, consistent with dominant gain of function.[12,17] Lifelong expression of gain-of-function mutations, such as the UBE3A^{T485A} mutation that hyperactivates ubiquitin ligase activity,[12] will persistently target substrates for ubiquitination in a manner that is biochemically distinct from the WT enzyme.

Our bulk RNA-seq and scRNA-seq data indicate that maternal or paternal transmission of the *Ube3a*^{T503A} gain-of-function mutation alters gene expression early in development and throughout life. Our bulk RNA-seq showed an upregulation of interneuron markers at E14.5 in all three mutant genotypes (Figure 5A), and genes in cluster 1 were significantly enriched for markers of Int2 cells (hypergeometric test, $p = 2.67 \times 10^{-64}$). Likewise, GABAergic interneurons (Int2) that expressed high levels of *Zcchc12* were increased in mice of all three *Ube3a*^{T503A} genotypes at E14.5 and then normalized to WT levels by P0 (Figures 6B and S5B). Whether this increase reflects early maturation, early migration, and/or transient expansion will require future studies. Regardless, our bulk RNA-seq data, collected from all three mutant genotypes, scRNA-seq data, and HCR data independently support increased numbers of Int2-lineage interneurons embryonically in *Ube3a*^{T503A} mutant mice. Our observation is in line with the critical period theory associated with UBE3A function observed in AS mouse models. Specifically, a study showed that reinstatement of UBE3A expression at the embryonic stage, but not at the postnatal stages, fully rescued neurobehavioral deficits in AS mice.[34]

A recent study found that an excess of GABAergic neurons were produced in human cortical organoids when three different autism risk genes, *SUV420H1*, *ARID1B*, and *CHD8*, were individually mutated.[37] Precocious development and/or embryonic overproduction of GABAergic interneurons may represent a conserved cellular feature of many forms of autism and has the potential to alter excitatory-inhibitory balance[38] and impair brain development during specific critical periods.[39] Int2 interneurons expressed *Sst* and *Calb2* embryonically (Figure 6D), suggesting that they may give rise to somatostatin- and calbindin2/calretinin-expressing interneurons later in life. Indeed, our HCR data suggested that *GAD2*$^{+}$/*Zcchc12*$^{+}$ cells mature into *Sst*$^{+}$ and *Calb2*$^{+}$ interneurons by P24. Future studies will be needed to evaluate the extent to which the function of these interneuron subtypes is affected in adult *Ube3a*^{T503A} mutant mice.

While increasing evidence suggests that paternally inherited UBE3A gain of function causes neurodevelopmental disorders,[11,17] most of the affected individuals with UBE3A gain-of-function mutations harbor the mutation on the maternal allele,[17] similar to AS and Dup15q disorders. Identification of new clinical cases and characterization of additional mouse models will be needed to further explore the relationship between parent of origin and phenotypic severity. Our data reveal that neurobehavioral deficits in patT503A mice

are distinct from those of matT503A or homoT503A mice, suggesting that parent of origin can influence the spectrum of phenotypes caused by UBE3A gain-of-function mutations. Differences might relate to the expression of a dominant UBE3A allele in mitotic cells, where both alleles are expressed, vs. mature neurons, where the maternal allele is primarily expressed.[4]

Our data also indicate that UBE3A gain of function results in distinct behavioral deficits when compared with AS. HomoT503A and matT503A mutant mice were hyperactive, as demonstrated by open-field and three-chamber social tests. This contrasts with AS model mice, which are hypoactive in the open-field test, as reproduced by multiple labs.[25,35,36,40–42] In addition, deficits in marble-burying tests and reduced motor coordination are commonly observed in AS mice.[25,35,36,40–42] In contrast, neither marble-burying deficits nor impairment in motor coordination were observed in matT503A, patT503A, or homoT503A mice. Instead, matT503A mice displayed enhanced performance on the rotarod. A larger proportion of matT503A and homoT503A mice reached the 300 s cutoff in the rotarod assay relative to WT mice, suggesting that their performance was enhanced, although use of a longer cutoff time will be needed in the future to avoid a "ceiling effect."

Collectively, our study and Weston et al.[17] indicate that UBE3A gain-of-function mutations increase risk for one or more new neurodevelopmental disorders, with symptoms that are distinct from AS, a UBE3A loss-of-function disorder. Going forward, whenever another UBE3A missense mutation is identified in a patient, the following aspects need to be carefully assessed for accurate diagnosis and intervention. First, it is important to ascertain if the mutation causes loss or gain of function, using previously described approaches.[13,17] Note that a reduction in UBE3A protein level should not be used as an indicator for UBE3A loss of function because UBE3A gain-of-function mutations also result in reduced UBE3A protein levels, as demonstrated in this and previous studies.[12,17] However, gain or loss of function of UBE3A can be assessed by examining its effects on additional UBE3A substrates. Secondly, the parental origin of each UBE3A mutation needs to be determined. This can be achieved by genotyping and pedigree analysis or by haplotype phasing, as we did in this study. Lastly, all symptoms need to be carefully documented. Given that the spectrum of phenotypes differed when these gain-of-function mutations were maternally or paternally inherited in mice and in humans,[17] we hypothesize that UBE3A gain-of-function mutations will cause one or more distinct syndromic disorders in humans, with symptoms and penetrance that vary by parent of origin and the degree to which the mutation hyperactivates UBE3A.

Limitations of the study

A limitation of this study is that most experiments were performed with male mice, including longitudinal RNA-seq and neurobehavioral studies. Sex-dependent phenotypes were reported in AS model models.[43,44] Whether female *Ube3a*^{T503A} mice show similar phenotypes will require future studies. Deficits in the three-chamber sociability test, as seen in patT503A mutant mice, are frequently interpreted as an impairment in sociability. Subtle changes in anxiety, sensorimotor functions, or even deficits outside the nervous system could

also impair behavior in this assay. In addition, our studies were focused on the C57BL/6 mice. Mouse genetic background can influence phenotypic severity in AS mouse models[35] and other autism model mice,[45] so future studies with mutant mice on different genetic backgrounds will help to fully understand the phenotypic spectrum caused by UBE3A gain-of-function mutations.

STAR★METHODS

RESOURCE AVAILABILITY

Lead contact—Further information and requests for resources and reagents should be directed to and will be fulfilled by the lead contact, Mark J. Zylka (zylka@med.unc.edu).

Materials availability—Requests for *Ube3a*^{T503A} mice and plasmids generated in this study should be directed to the lead contact.

Data and code availability

- Bulk and single-cell RNA-seq data were deposited to Gene Expression Omnibus: GSE201734.
- All code used for analysis of the scRNA-seq data is available at GitHub: (https://doi.org/10.5281/zenodo.8007301) https://github.com/jeremymsimon/Xing_Ube3a/tree/V1.0.
- Any additional information required to reanalyze the data reported in this work paper is available from the lead contact upon request.

EXPERIMENTAL MODEL AND STUDY PARTICIPANT DETAILS

Mouse models—All animal procedures in this study were approved by the Institutional Animal Care and Use Committee at the University of North Carolina at Chapel Hill. *Ube3a*^{T503A} mice were generated in C57BL/6J blastocysts using CRISPR/Cas9 insertional mutagenesis by the UNC Animal Model Core facility. This mouse mutation precisely models the human *UBE3A*^{T485A} mutation; numbering based on human isoform 1. The founder line was backcrossed with WT C57BL/6J mice, purchased from Jackson Laboratories, for two generations prior to establishing the *Ube3a*^{T503A} colony. Backcrossing removes unlinked, random mutations that might have been introduced by CRISPR/Cas9. In this study, we intercrossed heterozygous mutant mice to generate homozygous mutant mice (*Ube3a*$^{pT503A/mT503A}$, homoT503A). Paternal heterozygous mutant mice (*Ube3a*$^{pT503\ A/m+}$, patT503A) and littermate control mice were generated by breeding homozygous or heterozygous mutant males with WT females. Maternal heterozygous mutant mice (*Ube3a*$^{p+/mT503A}$, matT503A) were generated by breeding WT males with heterozygous or homozygous females. All embryonic and P0 biochemistry and histology studies were conducted on mutant mice with littermate controls. Studies on adult mice were performed on age-matched mutants and controls. Mice from multiple litters were used per group to rigorously control for litter effects.[26] Genomic DNA was extracted from tail or ear samples and utilized for genotyping by polymerase chain reaction (PCR). Homo- and/or heterozygosity of *Ube3a*^{T503A} and *Ube3a*^{WT} alleles was determined by

PCR utilizing primers (listed 5′−3′) *Ube3aT503A*-F: CCTCGAGTGGATCCACTAGAA and *Ube3aT503A*-R: CATTAGACAACCAGGATACCAGT, followed by *AluI* restriction enzyme digestion. Sex of embryos and P0 mice was determined by PCR using *Sry*-F:TCATGAGACTGCCAACCACAG and *Sry*-R: CATGACCACCACCACCACCAA primer pairs.

Ube3a knock-out mice[23] were maintained on the C57BL/6 background in the lab. $Ube3a^{m-/p+}$ (AS) and littermate control (WT) mice were generated by breeding WT males with $Ube3a^{-/+}$ females. The following primers were used to identified mutant and WT *Ube3a* alleles: *Ube3a*-F1: ACTTCTCAAGGTAAGCTGAGCTTGC, *Ube3a*-F2: TGCATCGCATTGTGTGAGTAGGTGTC and *Ube3a*-R: GCTCA AGGTTGTATGCCTTGGTGCT.

Cell lines—HEK293T cells were obtained from ATCC and maintained in DMEM/FBS.

METHOD DETAILS

Western Blot—Freshly dissected whole cortex from one hemisphere of each animal was extracted in 1X RIPA buffer (25 mM Tris-HCl pH 7.5, 150 mM NaCl, 1% NP-40, 1% sodium deoxycholate, 0.1% SDS) supplement with 1X phosphatase inhibitor cocktail (Sigma-Aldrich, P5726) and 1X protease inhibitor cocktail (Sigma-Aldrich, P8340). Total protein lysates were prepared by sonication using a Fisher Scientific Sonic Dismembrator Model 500 equipped with a microtip at 50% amplitude on ice with 2 × 15s pulses, and cleared by centrifugation at 20,000 g at 4°C for 10 min. Protein concentration was determined using Bio-Rad Protein Assay (Bio-Rad, 5000006) against BSA protein standards. An equal amount of total protein was resolved in a 4–15% precast SDS/PAGE gel (Bio-Rad, 4568094) and transferred to PVDF membranes (Bio-Rad, 1620174) for Western blot analyses. Membranes were blocked with Intercept (PBS) blocking buffer (LI-COR, 927–70001) for 30 min and incubated with primary antibodies diluted in blocking buffer supplemented with 0.1% Tween 20 for 1 h at room temperature or overnight at 4°C. Membranes were washed with Phosphate-buffered saline (PBS) supplemented with 0.1% Tween 20 (PBS/T) three times and incubated with IRDye 680RD-conjugated donkey anti-mouse polyclonal antibody (LI-COR, c6116–05; 1:10,000) and/or IRDye 800CW-conjugated donkey anti-rabbit (LI-COR, c60712–05; 1:10,000) diluted in blocking buffer at room temperature for 1 h at room temperature. Membranes were washed with PBS/T 3 times and scanned using an Odyssey CLx infrared imaging system (LI-COR Biosciences). Primary antibodies used for Western blot are: mouse anti-UBE3A (Sigma-Aldrich, SAB1404508; 1:1,000), rabbit anti-PSMD4 (Cell Signaling, 3846; 1:1,000), rabbit anti-PSMD1 (Atlas antibodies, HPA036736; 1:500), rabbit anti-PSMA2 (ThermoFisher Scientific, PA5–17294; 1:1,000), mouse anti-ERK3 (ThermoFisher Scientific, MA1101; 1:300), rabbit anti-NEURL4 (ThermoFisher Scientific, PA563108, 1:300), rabbit anti-PSMB1 (ThermoFisher Scientific, PA5–49648; 1:1,000), rabbit anti-RAD23A (Proteintech, 51033–1-AP; 1:1000), mouse anti-β-ACTIN (Sigma-Aldrich, A1978; 1:5,000), mouse anti-Myc tag (Millipore, 05–724; 1:3,000), rabbit anti-GFP (Novus, NB600–308; 1:2,000). Western blot signals of proteins of interest were measured in ImageJ and normalized to β-ACTIN for comparisons. Relative levels of UBE3A (mean ± s.e.m.) to WT were shown

below representative blots in the Figure legends. Both male and female mice were used for Western blot analyses.

DNA constructs and luciferase assay—All UBE3A expression plasmids used in this study were constructed based on human UBE3A isoform I (NCBI Reference Sequence: NP_001361390.1) with myc epitope tags placed on the N terminus of UBE3A by PCR and cloned into pCIG2 using *SacI* and *XmaI* sites. The UBE3A^{T787A} point mutation was introduced by site-directed mutagenesis using primers (listed as 5′−3′) CTTGCAGTTTACAGCGGGCACAGACAG and CTGTCTGTGCCCGCTGTAAACTGCAAG. All constructs were verified by Sanger sequencing.

β-catenin-activated reporter (BAR) assays were performed as described with minor modifications.[13] HEK293T cells were plated at a density of 10,000/well in 96-well plates. Cells were transiently transfected with 10 ng of pRL-TK-Renilla luciferase, 30 ng of BAR-pGL3, and 60 ng of pCIG empty vector or UBE3A-expressing constructs using 1 μL of Fugene6 transfection reagent (Promega, E2691) mixed in Opti-MEM (Invitrogen). 24 h after transfection, BAR (Firefly) and Renilla luciferase activity was assessed using the Dual-Luciferase reporter assay system (Promega) according to the manufacturer's suggested protocol. Luciferase activities were measured using a CLAROstar^{plus} plate reader (BMG Labtech). BAR luciferase activity was normalized against Renilla activity for comparison.

Brain section preparation and immunolabeling—Adult male mice were anesthetized and perfused transcardially with 4% paraformaldehyde (PFA) prepared in 1X PBS and brains were dissected and postfixed in 4% PFA for 16 h. P0 mice were decapitated and brains were dissected and drop-fixed in 4% PFA for 24 h. Brains were embedded in 4% low-melting-point agarose in 1X PBS and sectioned using a Leica VT1200 vibratome. Sections were stored in 1X PBS at 4°C before immunolabeling.

For immunolabeling, sections were rinsed in 1X PBS and incubated in blocking solution (5% normal donkey serum, 0.3% Triton X-100, 2% DMSO, 0.02% Sodium Azide in 1X PBS) at room temperature. Primary antibodies were diluted in blocking solution and incubated overnight at room temperature. The following antibodies and conditions were utilized for immunolabeling: mouse anti-UBE3A (Sigma-Aldrich, SAB1404508; 1:1,000), guinea pig anti-NEUN (Millipore, ABN90P; 1:1,000), rabbit anti-CUX1 (Santa Cruz, sc-13024; 1:500), rat anti-CTIP2 (Abcam, ab18465; 1:1,000), rabbit anti-PSMD4 (Cell Signaling; 3846, 1:500), rabbit anti-PAX6 (BioLegend, 901301, 1:500), and rabbit anti-OLIG2 (Millipore, AB9610; 1:2,000). Brain sections were rinsed in 0.1% Triton X-100/1 X PBS (PBS/T) three times and incubated with secondary antibodies in blocking solution for 3 h at room temperature. Secondary antibodies utilized include donkey anti-rabbit IgG Alexa Fluor 568 (ThermoFisher Scientific, A10042; 1:1,000), goat anti-rat IgG Alexa Fluor 488 (ThermoFisher Scientific, A11006; 1:1,000), goat anti-mouse IgG2a Alexa Fluor 488 (ThermoFisher Scientific, A21131; 1:1,000) and donkey anti-guinea pig IgG Alexa 647 (Jackson ImmunoResearch, 706–605-148; 1:1,000). Sections were then stained with DAPI (1:1,000 in PBS/T) and rinsed with PBS/T three times for 20 min each. Sections were mounted onto Fisherbrand Superfrost/Plus slides (Fisher Scientific) using antifading

Polyvinyl alcohol mounting medium with DABCO (Sigma-Aldrich, 10981). Images were collected with Zeiss LSM 710 or LSM 780 laser scanning confocal microscopes.

Hybridization chain reaction—E14.5 and P0 brains from both male and female mice were drop-fixed in 4% PFA for 24 h and P24 brains were dissected from PFA perfused animals and postfixed in 4% PFA for 24 h. All brains were then incubated in 30% sucrose/PBS at 4°C for 48 h, and embedded in O.C.T. compound. Cryostat sections were collected at 30 μm and mounted on Fisherbrand Superfrost Plus slides and air-dried prior to mRNA detection by HCR.

HCR was performed according to the protocol provided by the manufacturer (Molecular Instruments) except hairpins for signal amplification were used at 1/5 of the suggested amount. Pre-designed HCR probe sets for mouse *GAD2* with B1 amplifier, *Zcchc12* with B3 amplifier, *Calb2*, *Sst* and *Pvalb* with B5 amplifier were purchased from Molecular Instruments, Inc. B1 amplifier coupled with Alexa Fluor 488, B5 amplifier coupled with Alexa Fluor 546 and B3 amplifier coupled with Alexa Fluor 647 were pre-designed by the manufacturer. Images were collected with Zeiss LSM 710 or LSM 780 laser scanning confocal microscopes.

Confocal image analysis—Confocal images of the somatosensory cortex were collected for fluorescence intensity, cortex or layer thickness, and cell number analyses. Images were acquired from anatomically matched coronal sections along the rostral-caudal axis. For cortical thickness analyses, cortical layers were determined by the distribution of cortical upper layer (layer 2–4) marker, CUX1, and deeper layer (layer 5–6) marker, CTIP2. The thickness of different cortical layers was measured along the middle segment of selected regions of interest (ROIs). For cell number assessment, images were processed using ImageJ. Briefly, images were auto-thresholded at the default setting with manual adjustment to eliminate unfocused signals and binary images were created and watershedded. Numbers of $CUX1^+$ cells in upper layers and $CTIP2^+$ cells in deeper layers were automatically determined using the Analyze Particles function with a cut-off size at 17.5 μm^2.

To measure UBE3A and PSMD4 fluorescent intensity, all images were thresholded in ImageJ. Masks of NEUN signals were created representing total neuronal areas including both nuclear and cytoplasmic compartments. Masks of DAPI signals were created as the nuclear compartment. Masks representing the cytoplasmic compartment were created by subtracting nuclear compartments from total neuronal areas. Averaged fluorescent signals of UBE3A and PSMD4 in each compartment were measured. Masks of OLIG2 signals were created to measure signals of UBE3A in the nuclear compartment of oligodendrocytes. Two to three ROIs from each animal were analyzed and results were averaged for statistical analyses.

To quantify *Zcchc12*$^+$ expressing interneurons, z stack images were acquired across the depth of 1 μm at 0.2 μm/step using a 60× objective with 1.2× zoom. Images obtained after maximum intensity projection were used for cell counting. HCR signals were thresholded via background adjustment and particle size exclusion (≥ 20 pixels) in ImageJ. *GAD2*$^+$ and *Zcchc12*$^+$ cells were manually counted in Photoshop using the Count tool. Individual

GAD2^{+} and *Zcchc12*$^{+}$ cells were identified against DAPI signals and cells with ≥1 particles in the *GAD2* channel were counted as *GAD2*$^{+}$ cells and cells with ≥ 5 particles in the *Zcchc12* channel were counted as *Zcchc12*$^{+}$ cells. The percentage of *Zcchc12*$^{+}$/*GAD2*$^{+}$ cells from 2 to 3 ROIs for each animal were averaged for comparison.

All representative images were cropped and adjusted for brightness and contrast in Photoshop for presentation. Mice from a minimum of three litters were analyzed for each experiment.

Behavior assessments—Homozygous, paternal heterozygous, and maternal heterozygous mutant male mice were accessed separately, but the same timeline for behavioral tests was used. Each cohort contained 12 to 14 mice of one mutant genotype and an equal number of age-matched WT mice. All mouse behavioral tests were performed at The UNC Mouse Behavioral Phenotyping Core facility according to established standard protocols as described below.

Open-field test—Open-field test was used to evaluate the exploratory activity and anxiety-like behavior of a mouse in a novel environment. The test was conducted as a 1-h trial in an open-field chamber (41 cm × 41 cm × 30 cm) equipped with a grid of photobeams (VersaMax, AccuScan Instruments). Mouse body position and movements were tracked as photobeams broke during the trial. Both locomotion (total distance traveled) and vertical rearing movements were measured. Time spent in the center zone of the open-field chamber was used to evaluate levels of anxiety-like behavior.

Elevated plus-maze for anxiety-like behavior—The test was conducted as a 5-min trial on a plus-maze for each mouse. The plus-maze was constructed with two closed arms and two open arms. The total time spent in and entries to the open and closed arms were measured.

Three-chamber sociability and social novelty tests—Social preference of a mouse was evaluated in a three-chamber choice task. The whole task contains two components: sociability test and social novelty test. The sociability test was used to evaluate a mouse's preference for a social object over a non-social object and the social novelty test was used to evaluate a mouse's preference for a novel unfamiliar social object over a familiar social object. All tests were conducted in a rectangular apparatus fabricated from clear Plexiglas. The apparatus was divided into three chambers connected by doorways. The movement of a mouse were tracked and analyzed using the Noldus Ethovision video tracking system. Before the sociability test, the test subject was put in the center chamber and allowed to explore all three empty chambers freely for 10 min. Then, the sociability test was conducted. The test subject was first confined to the center chamber with both doorways closed. An empty wire cage was then placed in one side chamber and an identical wire cage containing an unfamiliar, sex-matched mouse (Stranger #1) was placed in the other side chamber. The doorways were then re-opened, and the test subject was allowed to freely explore the testing chambers for 10 min. Upon the completion of sociability test, the test subject was further evaluated for social novelty preference. With the test subject confined in the center chamber, and a second unfamiliar, sex-matched mouse (Stranger #2) was placed into the empty wire

cage. The chamber doorways were then re-opened, and the test subject was allowed to freely explore the testing chambers for 10 min. For both sociability and social novelty tests, time spent in close proximity to and entries into each side chambers were measured.

Accelerating rotarod test—The test was performed using an accelerating rotarod assembly (Ugo Basil, Italy) where mice are placed on a cylinder which slowly accelerates from 3 revolutions per minute (rpm) to a maximum of 30 rpm across a maximum trial length of 5 min (300 s). The entire test for each mouse was conducted in two sessions. For the first session, 3 trials were performed with an interval of 45 s between trials. The second session was conducted two days after the completion of the first session to evaluate motor learning. Two trials were given with an interval of 45 s in the second session. Latency to fall from the rotating cylinder was measured.

Marble-burying assay—The marble burying assay was conducted in a Plexiglas cage with 5 cm deep of corncob bedding. On top of the bedding, 20 black glass marbles were evenly arranged as a 5 × 4 grid on top of the bedding. The total number of marbles buried in 30 min was measured.

Acoustic startle and prepulse inhibition—Prepulse inhibition of a startle response was used to evaluate the function of auditory system and sensorimotor gating in mice. The test was conducted using an SR-Lab-Startle Response system (San Diego Instruments) equipped with a large sound-attenuating cabinet with a ceiling light, fan, and a loudspeaker for the acoustic stimuli. In the test cabinet, mice were placed in a small Plexiglas cylinder seated on a piezoelectric transducer to record the vibration caused by mouse startle responses. Seven different types of trials were presented in this test, including no-stimulus trials, trials with the 40 ms acoustic startle stimulus at 120 dB alone, and trials with a 20 ms prepulse stimulus at 74, 78, 82, 86, or 90 dB presented 100 ms before the onset of the startle stimulus (40 ms, 120dB). The test session consisted of total 42 trials presented in blocks of 7 trials. Each block started with a 5-min habituation period followed by 7 trials in randomized order, with an average interval of 15 s (range: 10 to 20 s) between trials. The peak response within 65 ms sampling window from the onset of the startle stimulus was used as the measure of a startle amplitude. Levels of percent prepulse inhibition were measured and compared as the function of genotypes.

Test for olfactory function—Olfactory function of a mouse was evaluated by its ability to retrieve a food reward buried in the cage bedding. Two or three days before the test, unfamiliar food pellets (Froot Loops, Kellogg’s Co.) were placed overnight in the home cage of the test subject. Consumptions of the novel food were observed to ensure that the novel food is a valid food reward to the test subject. About 16–20 h before the test, all food was removed from the home cage. The test was performed in a large, clean tub cage with 3 cm deep paper chip bedding. Each test subject was first allowed to explore the cage for 5 min and after the test subject was removed, one piece of the food reward was buried in the bedding. The animal was then returned to the cage and the time taken to find the food reward was measured. A maximum of 15 min was allowed for the test subject to find the food reward.

Hot-plate test—Thermal and/or pain sensitivity was tested on a horizontal hot plate surface heated to 55°C. The temperature was precisely controlled by an IITChot plate apparatus. For this test, the test subject was placed in a tall transparent plastic cylinder on the hot plate and observed for any reaction to the heated surface, such as licking a hindpaw, jumping or vocalizations. The test subject was immediately removed if any reaction to the hot plate was observed. The maximum length for this test was 30 s. The latency to respond to the hot plate was measured.

RNA extraction, sequencing and analysis—Brains of mice (male only) sacrificed at the embryonic day (E)14.5 and at 1, 6, and 12 months of age were removed, and the cerebral cortex (one hemisphere) was dissected and stored at −80°C. Six replicates per time point were collected for both WT and mutant mice of each genotype for a total of 96 samples. All samples were processed in parallel as described previously, including RNA extraction, library construction, RNA sequencing and data analyses.[33] Libraries were prepared using the KAPA mRNA preparation kit and sequenced on an Illumina HiSeq4000 as stranded, paired-end, 50 bp reads. Reads were filtered for a quality score of 20 or more in at least 90% of all bases using fastq_quality_filter in the FASTX toolkit 0.0.14 (http://hannonlab.cshl.edu/fastx_toolkit/index.html). Sequencing adapters were trimmed using cutadapt 1.12,[46] and reads were then aligned to the mm9 reference genome using STAR 2.5.2b.[47] Transcripts were quantified using Salmon 0.11.3,[48] and differential expression was detected using DESeq2 1.22.2,[49] using a model that corrected for batch effects and a threshold of adjp <0.05.

Hierarchical clustering of RNA-seq data from bulk tissue and pathway analyses—We first created a union set of differentially expressed genes from all four mouse ages assayed. Fold-changes were standardized and constrained to a scale of −1 to +1 by dividing the fold-change by the maximum absolute fold-change value for that gene across all four time points. Genes were then clustered hierarchically using 1–Pearson correlation distance. The resulting tree was cut at a height of 1.75, resulting in 9 gene clusters. The genes were then filtered to remove those with Pearson correlation <0.5. To determine which pathways were enriched among the 9 clusters, we used gprofiler2.[50] Pathways were considered significant at adjusted p value <0.05.

Single-cell RNA sequencing and data processing—Single cell RNA sequencing (Drop-seq)[51] was performed on cortices from E14.5 and P0 WT and homoT503A mice (WT E14.5, n = 6; homoT503A E14.5, n = 5; WT P0, n = 3; homoT503A P0, n = 5). WT and mutant samples were performed in parallel. Single cell isolation and sequencing were performed as described in our previous publication,[27] where data from WT samples were previously reported. Each replicate contained cortical cells from male and female littermates. cDNA from an estimated 12,000 E14.5 cells and 8,000 P0 cells were pooled, purified and tagmented with Nextera XT DNA Library Preparation kit (Illumina). Input cDNA (1 ng) from each replicate was amplified with custom primer P5_TSO_Hybrid and Nextera index primers (Table S1). Tagmented samples were purified twice with 0.6 × and 1 × AMPure XP beads. All replicates were pooled and sequenced on one Illumina HiSeq 4000 flowcell (eight lanes) to avoid sequencing bias. Read 1 was 20 bp; bases 1–12 represent the

cell barcode, bases 13–20 represent the UMI. Read 2 was 50 bp and Read 3 (sample index) was 8 bp. Samples were de-multiplexed using bcl2fastq version 2.18.0.12.

Identification of cells and quantification of transcript abundance was performed using Alevin.[52] These gene expression matrices (one per genotype, time point, and replicate) were then imported into Seurat version 3.1 using tximport[53] and cells were filtered such that they had to contain at least 2,000 UMIs, had between 1,000 and 6,000 genes detected, and less than 5% contribution by mitochondrial or hemoglobin transcripts. Each biological sample was normalized and scaled using sc Transform v1,[54] then integrated together using Seurat with 5,000 anchors. Dimensionality reduction was conducted using the top 100 principal components. Cell types were identified using Louvain-Jaccard clustering with multilevel refinement and resolution = 2. Proportional shifts between genotypes in each cluster were detected using the propeller method[55] with arcsin square root transformation and differences were considered significant at Benjamini-Hochberg FDR <0.05. Pseudotiming was performed on the interneuronal lineage (clusters annotated as ganglionic eminences or interneurons) using Slingshot.[56] The data were subset to genes identified as markers of these clusters (via Seurat FindAllMarkers on the RNA assay with log-fold-change threshold = 1), and a new UMAP projection was computed based on the integrated data for these cells and genes. Then slingshot was executed specifying clusters 5 and 7 as possible termini of the trajectories. Significantly temporally expressed genes were then detected using tradeSeq[57] where a negative binomial generalized additive model was fit to the data in the RNA assay. Genes were considered statistically significant if the adjusted p value was less than 0.05 for either of the two lineages. Heatmaps and scatterplots were then generated in R using ComplexHeatmap[58] and ggplot2.

QUANTIFICATION AND STATISTICAL ANALYSIS

For all experiments, n represents the number of animals. All statistical analyses were performed in GraphPad Prism 9.3.1 and results were reported in figure legends. Results were presented as the mean +/− standard error of the mean (s.e.m.). Differences were considered significant when $p < 0.05$. p values are listed over bar graphs or in the coresponding figure legends. Except for mouse behavior tests, Student's *t*-tests or paired *t*-tests were used for comparisons of two groups and one-way ANOVA analyses with *post hoc* Tukey's tests were used for comparisons of three or more groups.

Results from behavioral tests were analyzed using two-way, or repeated measures Analysis of Variance (ANOVA). *post hoc* Bonferroni's multiple comparisons tests were used for comparing group means only when a significant F value was determined in the overall ANOVA for open-field tests. Uncorrected Fisher's LSD tests were used as post hoc analyses for rotarod tests. Tukey's multiple comparisons tests were used as post hoc analyses to determine side preference in the three-chamber social approach test. For all comparisons, significance was set at $p < 0.05$.

Supplementary Material

Refer to Web version on PubMed Central for supplementary material.

ACKNOWLEDGMENTS

We thank Ralf S. Schmid and Ben W. Rees for technical assistance. This work was supported by a grant from the NIH-NIMH (5R01MH120229) to M.J.Z. Confocal imaging was conducted at the UNC Neuroscience Microscopy Core (RRID:SCR_019060), supported, in part, by funding from NIH-NINDS Neuroscience Center Support Grant P30 NS045892 and NIH-NICHD grant P50 HD103573. J.M.S. and T.S.P. were supported by NIH-NICHD (U54HD079124) and NIH-NINDS (P30 NS045892). The mouse model was generated by the UNC Animal Models Core Facility, supported in part by a Cancer Center Core Support Grant (P30CA016086) to the UNC Lineberger Comprehensive Cancer Center. We thank Drs. Sheryl S. Moy, Viktoriya D. Nikolova, and Natallia V. Riddick for their help with mouse behavior tests. Mouse behavioral experiments were conducted by The UNC Mouse Behavioral Phenotyping Core, which was supported by an NIH-NICHD grant (P50 HD103573; PI: Gabriel Dichter).

INCLUSION AND DIVERSITY

We support inclusive, diverse, and equitable conduct of research.

REFERENCES

1. de Bie P, and Ciechanover A (2011). Ubiquitination of E3 ligases: self-regulation of the ubiquitin system via proteolytic and non-proteolytic mechanisms. Cell Death Differ. 18, 1393–1402. 10.1038/cdd.2011.16. [PubMed: 21372847]
2. Margolis SS, Sell GL, Zbinden MA, and Bird LM (2015). Angelman Syndrome. Neurotherapeutics 12, 641–650. 10.1007/s13311-015-0361-y. [PubMed: 26040994]
3. Owais A, Mishra RK, and Kiyokawa H (2020). The HECT E3 LigaseE6AP/UBE3A as a Therapeutic Target in Cancer and Neurological Disorders. Cancers 12, 2108. 10.3390/cancers12082108. [PubMed: 32751183]
4. Judson MC, Sosa-Pagan JO, Del Cid WA, Han JE, and Philpot BD (2014). Allelic specificity of Ube3a expression in the mouse brain during postnatal development. J. Comp. Neurol. 522, 1874–1896. 10.1002/cne.23507. [PubMed: 24254964]
5. Kishino T, Lalande M, and Wagstaff J (1997). UBE3A/E6-AP mutations cause Angelman syndrome. Nat. Genet. 15, 70–73. 10.1038/ng0197-70. [PubMed: 8988171]
6. Kalsner L, and Chamberlain SJ (2015). Prader-Willi, Angelman, and 15q11-q13 Duplication Syndromes. Pediatr. Clin. 62, 587–606. 10.1016/j.pcl.2015.03.004.
7. Khatri N, and Man HY (2019). The Autism and Angelman Syndrome Protein Ube3A/E6AP: The Gene, E3 Ligase Ubiquitination Targets and Neurobiological Functions. Front. Mol. Neurosci 12, 109. 10.3389/fnmol.2019.00109. [PubMed: 31114479]
8. Lusk L, Vogel-Farley V, DiStefano C, and Jeste S (1993). Maternal 15q Duplication Syndrome. In GeneReviews((R)), Adam MP, Ardinger HH, Pagon RA, Wallace SE, Bean LJH, Gripp KW, Mirzaa GM, and Amemiya A, eds.
9. Urraca N, Cleary J, Brewer V, Pivnick EK, McVicar K, Thibert RL,Schanen NC, Esmer C, Lamport D, and Reiter LT (2013). The interstitial duplication 15q11.2-q13 syndrome includes autism, mild facial anomalies and a characteristic EEG signature. Autism Res. 6, 268–279. 10.1002/aur.1284. [PubMed: 23495136]
10. Noor A, Dupuis L, Mittal K, Lionel AC, Marshall CR, Scherer SW, Stockley T, Vincent JB, Mendoza-Londono R, and Stavropoulos DJ (2015). 15q11.2 Duplication Encompassing Only the UBE3A Gene Is Associated with Developmental Delay and Neuropsychiatric Phenotypes. Hum. Mutat. 36, 689–693. 10.1002/humu.22800. [PubMed: 25884337]
11. Iossifov I, O'Roak BJ, Sanders SJ, Ronemus M, Krumm N, Levy D, Stessman HA, Witherspoon KT, Vives L, Patterson KE, et al. (2014). The contribution of de novo coding mutations to autism spectrum disorder. Nature 515, 216–221. 10.1038/nature13908. [PubMed: 25363768]
12. Yi JJ, Berrios J, Newbern JM, Snider WD, Philpot BD, Hahn KM, and Zylka MJ (2015). An Autism-Linked Mutation Disables Phosphorylation Control of UBE3A. Cell 162, 795–807. 10.1016/j.cell.2015.06.045. [PubMed: 26255772]

13. Yi JJ, Paranjape SR, Walker MP, Choudhury R, Wolter JM, Fragola G, Emanuele MJ, Major MB, and Zylka MJ (2017). The autism-linked UBE3A T485A mutant E3 ubiquitin ligase activates the Wnt/beta-catenin pathway by inhibiting the proteasome. J. Biol. Chem. 292, 12503–12515. 10.1074/jbc.M117.788448. [PubMed: 28559284]

14. Kühnle S, Martínez-Noël G, Leclere F, Hayes SD, Harper JW, and Howley PM (2018). Angelman syndrome-associated point mutations in the Zn(2+)-binding N-terminal (AZUL) domain of UBE3A ubiquitin ligase inhibit binding to the proteasome. J. Biol. Chem. 293, 18387–18399. 10.1074/jbc.RA118.004653. [PubMed: 30257870]

15. Avagliano Trezza R, Sonzogni M, Bossuyt SNV, Zampeta FI, Punt AM, van den Berg M, Rotaru DC, Koene LMC, Munshi ST, Stedehouder J, et al. (2019). Loss of nuclear UBE3A causes electrophysiological and behavioral deficits in mice and is associated with Angelman syndrome. Nat. Neurosci. 22, 1235–1247. 10.1038/s41593-019-0425-0. [PubMed: 31235931]

16. Buel GR, Chen X, Chari R, O'Neill MJ, Ebelle DL, Jenkins C, Sridharan V, Tarasov SG, Tarasova NI, Andresson T, and Walters KJ (2020). Structure of E3 ligase E6AP with a proteasome-binding site provided by substrate receptor hRpn10. Nat. Commun. 11, 1291. 10.1038/s41467-020-15073-7. [PubMed: 32157086]

17. Weston KP, Gao X, Zhao J, Kim KS, Maloney SE, Gotoff J, Parikh S, Leu YC, Wu KP, Shinawi M, et al. (2021). Identification of disease-linked hyperactivating mutations in UBE3A through large-scale functional variant analysis. Nat. Commun. 12, 6809. 10.1038/s41467-021-27156-0. [PubMed: 34815418]

18. Lee SY, Ramirez J, Franco M, Lectez B, Gonzalez M, Barrio R, and Mayor U (2014). Ube3a, the E3 ubiquitin ligase causing Angelman syndrome and linked to autism, regulates protein homeostasis through the proteasomal shuttle Rpn10. Cell. Mol. Life Sci. 71, 2747–2758. 10.1007/s00018-013-1526-7. [PubMed: 24292889]

19. Martínez-Noël G, Galligan JT, Sowa ME, Arndt V, Overton TM, Harper JW, and Howley PM (2012). Identification and proteomic analysis of distinct UBE3A/E6AP protein complexes. Mol. Cell Biol. 32, 3095–3106. 10.1128/MCB.00201-12. [PubMed: 22645313]

20. Kumar S, Talis AL, and Howley PM (1999). Identification of HHR23A as a substrate for E6-associated protein-mediated ubiquitination. J. Biol. Chem. 274, 18785–18792. 10.1074/jbc.274.26.18785. [PubMed: 10373495]

21. Cooper EM, Hudson AW, Amos J, Wagstaff J, and Howley PM(2004). Biochemical analysis of Angelman syndrome-associated mutations in the E3 ubiquitin ligase E6-associated protein. J. Biol. Chem. 279, 41208–41217. 10.1074/jbc.M401302200. [PubMed: 15263005]

22. Dagli AI, Mathews J, and Williams CA (1993). Angelman Syndrome. In GeneReviews((R)), Adam MP, Ardinger HH, Pagon RA, Wallace SE, Bean LJH, Gripp KW, Mirzaa GM, and Amemiya A, eds.

23. Jiang YH, Armstrong D, Albrecht U, Atkins CM, Noebels JL, Eichele G, Sweatt JD, and Beaudet AL (1998). Mutation of the Angelman ubiquitin ligase in mice causes increased cytoplasmic p53 and deficits of contextual learning and long-term potentiation. Neuron 21, 799–811. 10.1016/s0896-6273(00)80596-6. [PubMed: 9808466]

24. Judson MC, Burette AC, Thaxton CL, Pribisko AL, Shen MD, Rumple AM, Del Cid WA, Paniagua B, Styner M, Weinberg RJ, and Philpot BD (2017). Decreased Axon Caliber Underlies Loss of Fiber Tract Integrity, Disproportional Reductions in White Matter Volume, and Microcephaly in Angelman Syndrome Model Mice. J. Neurosci. 37, 7347–7361. 10.1523/JNEUROSCI.0037-17.2017. [PubMed: 28663201]

25. Wolter JM, Mao H, Fragola G, Simon JM, Krantz JL, Bazick HO,Oztemiz B, Stein JL, and Zylka MJ (2020). Cas9 gene therapy for Angelman syndrome traps Ube3a-ATS long non-coding RNA. Nature 587, 281–284. 10.1038/s41586-020-2835-2. [PubMed: 33087932]

26. Jiménez JA, and Zylka MJ (2021). Controlling litter effects to enhance rigor and reproducibility with rodent models of neurodevelopmental disorders. J. Neurodev. Disord. 13, 2. 10.1186/s11689-020-09353-y. [PubMed: 33397279]

27. Loo L, Simon JM, Xing L, McCoy ES, Niehaus JK, Guo J, Anton ES, and Zylka MJ (2019). Single-cell transcriptomic analysis of mouse neocortical development. Nat. Commun. 10, 134. 10.1038/s41467-018-08079-9. [PubMed: 30635555]

28. Guo J, and Anton ES (2014). Decision making during interneuron migration in the developing cerebral cortex. Trends Cell Biol. 24, 342–351. 10.1016/j.tcb.2013.12.001. [PubMed: 24388877]
29. Chen Y, Miles DK, Hoang T, Shi J, Hurlock E, Kernie SG, and Lu QR (2008). The basic helix-loop-helix transcription factor olig2 is critical for reactive astrocyte proliferation after cortical injury. J. Neurosci. 28, 10983–10989. 10.1523/JNEUROSCI.3545-08.2008. [PubMed: 18945906]
30. Cho G, Bhat SS, Gao J, Collins JS, Rogers RC, Simensen RJ, Schwartz CE, Golden JA, and Srivastava AK (2008). Evidence that SIZN1 is a candidate X-linked mental retardation gene. Am. J. Med. Genet. 146A, 2644–2650. 10.1002/ajmg.a.32472. [PubMed: 18798319]
31. Inoue T, Ota M, Ogawa M, Mikoshiba K, and Aruga J (2007). Zic1 and Zic3 regulate medial forebrain development through expansion of neuronal progenitors. J. Neurosci. 27, 5461–5473. 10.1523/JNEUROSCI.4046-06.2007. [PubMed: 17507568]
32. Kepecs A, and Fishell G (2014). Interneuron cell types are fit to function. Nature 505, 318–326. 10.1038/nature12983. [PubMed: 24429630]
33. Jimé nez JA, Ptacek TS, Tuttle AH, Schmid RS, Moy SS, Simon JM, and Zylka MJ (2020). Chd8 haploinsufficiency impairs early brain development and protein homeostasis later in life. Mol. Autism. 11, 74. 10.1186/s13229-020-00369-8. [PubMed: 33023670]
34. Silva-Santos S, van Woerden GM, Bruinsma CF, Mientjes E, Jolfaei MA, Distel B, Kushner SA, and Elgersma Y (2015). Ube3a reinstatement identifies distinct developmental windows in a murine Angelman syndrome model. J. Clin. Invest. 125, 2069–2076. 10.1172/JCI80554. [PubMed: 25866966]
35. Sonzogni M, Wallaard I, Santos SS, Kingma J, du Mee D, van Woerden GM, and Elgersma Y (2018). A behavioral test battery for mouse models of Angelman syndrome: a powerful tool for testing drugs and novel Ube3a mutants. Mol. Autism. 9, 47. 10.1186/s13229-018-0231-7. [PubMed: 30220990]
36. Tanas JK, Kerr DD, Wang L, Rai A, Wallaard I, Elgersma Y, and Sidorov MS (2022). Multidimensional analysis of behavior predicts genotype with high accuracy in a mouse model of Angelman syndrome. Transl. Psychiatry 12, 426. 10.1038/s41398-022-02206-3. [PubMed: 36192373]
37. Paulsen B, Velasco S, Kedaigle AJ, Pigoni M, Quadrato G, Deo AJ, Adiconis X, Uzquiano A, Sartore R, Yang SM, et al. (2022). Autism genes converge on asynchronous development of shared neuron classes. Nature 602, 268–273. 10.1038/s41586-021-04358-6. [PubMed: 35110736]
38. Rubenstein JLR, and Merzenich MM (2003). Model of autism: increased ratio of excitation/inhibition in key neural systems. Gene Brain Behav. 2, 255–267. 10.1034/j.1601-183x.2003.00037.x.
39. Wang DD, and Kriegstein AR (2009). Defining the role of GABA in cortical development. J. Physiol. 587, 1873–1879. 10.1113/jphysiol.2008.167635. [PubMed: 19153158]
40. Huang HS, Burns AJ, Nonneman RJ, Baker LK, Riddick NV, Nikolova VD, Riday TT, Yashiro K, Philpot BD, and Moy SS (2013). Behavioral deficits in an Angelman syndrome model: effects of genetic background and age. Behav. Brain Res. 243, 79–90. 10.1016/j.bbr.2012.12.052. [PubMed: 23295389]
41. Born HA, Dao AT, Levine AT, Lee WL, Mehta NM, Mehra S, Weeber EJ, and Anderson AE (2017). Strain-dependence of the Angelman Syndrome phenotypes in Ube3a maternal deficiency mice. Sci. Rep. 7, 8451. 10.1038/s41598-017-08825-x. [PubMed: 28814801]
42. Dutta R, and Crawley JN (2020). Behavioral Evaluation of Angelman Syndrome Mice at Older Ages. Neuroscience 445, 163–171. 10.1016/j.neuroscience.2019.10.027. [PubMed: 31730795]
43. Frohlich J, Miller MT, Bird LM, Garces P, Purtell H, Hoener MC,Philpot BD, Sidorov MS, Tan WH, Hernandez MC, et al. (2019). Electrophysiological Phenotype in Angelman Syndrome Differs Between Genotypes. Biol. Psychiatr. 85, 752–759. 10.1016/j.biopsych.2019.01.008.
44. Koyavski L, Panov J, Simchi L, Rayi PR, Sharvit L, Feuermann Y, and Kaphzan H (2019). Sex-Dependent Sensory Phenotypes and Related Transcriptomic Expression Profiles Are Differentially Affected by Angelman Syndrome. Mol. Neurobiol. 56, 5998–6016. 10.1007/s12035-019-1503-8. [PubMed: 30706369]

45. Tabbaa M, Knoll A, and Levitt P (2023). Mouse population genetics phenocopies heterogeneity of human Chd8 haploinsufficiency. Neuron 111, 539–556.e5. 10.1016/j.neuron.2023.01.009. [PubMed: 36738737]
46. Martin M (2011). Cutadapt removes adapter sequences from high-throughput sequencing reads. EMBnet. j. 17, 10–12. 10.14806/ej.17.1.200.
47. Dobin A, Davis CA, Schlesinger F, Drenkow J, Zaleski C, Jha S, Batut P, Chaisson M, and Gingeras TR (2013). STAR: ultrafast universal RNA-seq aligner. Bioinformatics 29, 15–21. 10.1093/bioinformatics/bts635. [PubMed: 23104886]
48. Patro R, Duggal G, Love MI, Irizarry RA, and Kingsford C (2017). Salmon provides fast and bias-aware quantification of transcript expression. Nat. Methods 14, 417–419. 10.1038/nmeth.4197. [PubMed: 28263959]
49. Love MI, Huber W, and Anders S (2014). Moderated estimation of fold change and dispersion for RNA-seq data with DESeq2. Genome Biol. 15, 550. 10.1186/s13059-014-0550-8. [PubMed: 25516281]
50. Kolberg L, Raudvere U, Kuzmin I, Vilo J, and Peterson H (2020). gprofiler2 – an R package for gene list functional enrichment analysis and namespace conversion toolset g:Profiler. F1000Res 9. 10.12688/f1000research.24956.2.
51. Macosko EZ, Basu A, Satija R, Nemesh J, Shekhar K, Goldman M, Tirosh I, Bialas AR, Kamitaki N, Martersteck EM, et al. (2015). Highly Parallel Genome-wide Expression Profiling of Individual Cells Using Nanoliter Droplets. Cell 161, 1202–1214. 10.1016/j.cell.2015.05.002. [PubMed: 26000488]
52. Srivastava A, Malik L, Smith T, Sudbery I, and Patro R (2019). Alevin efficiently estimates accurate gene abundances from dscRNA-seq data. Genome Biol. 20, 65. 10.1186/s13059-019-1670-y. [PubMed: 30917859]
53. Soneson C, Love MI, and Robinson MD (2015). Differential analyses for RNA-seq: transcript-level estimates improve gene-level inferences. F1000Res. 4, 1521. 10.12688/f1000research.7563.2. [PubMed: 26925227]
54. Hafemeister C, and Satija R (2019). Normalization and variance stabilization of single-cell RNA-seq data using regularized negative binomial regression. Genome Biol. 20, 296. 10.1186/s13059-019-1874-1. [PubMed: 31870423]
55. Phipson B, Sim CB, Porrello ER, Hewitt AW, Powell J, and Oshlack A (2022). propeller: testing for differences in cell type proportions in single cell data. Bioinformatics 38, 4720–4726. 10.1093/bioinformatics/btac582. [PubMed: 36005887]
56. Street K, Risso D, Fletcher RB, Das D, Ngai J, Yosef N, Purdom E, and Dudoit S (2018). Slingshot: cell lineage and pseudotime inference for single-cell transcriptomics. BMC Genom. 19, 477. 10.1186/s12864-018-4772-0.
57. Van den Berge K, Roux de Bézieux H, Street K, Saelens W, Cannoodt R, Saeys Y, Dudoit S, and Clement L (2020). Trajectory-based differential expression analysis for single-cell sequencing data. Nat. Commun. 11, 1201. 10.1038/s41467-020-14766-3. [PubMed: 32139671]
58. Gu Z, Eils R, and Schlesner M (2016). Complex heatmaps reveal patterns and correlations in multidimensional genomic data. Bioinformatics 32, 2847–2849. 10.1093/bioinformatics/btw313. [PubMed: 27207943]

Highlights

- UBE3A^{T503A} results in UBE3A gain of function *in vivo*
- UBE3A^{T503A} imposes long-lasting effects on gene expression
- Phenotypes in UBE3A^{T503A} mice are distinct from Angelman syndrome model mice
- Parental origin of UBE3A^{T503A} affects mouse behaviors

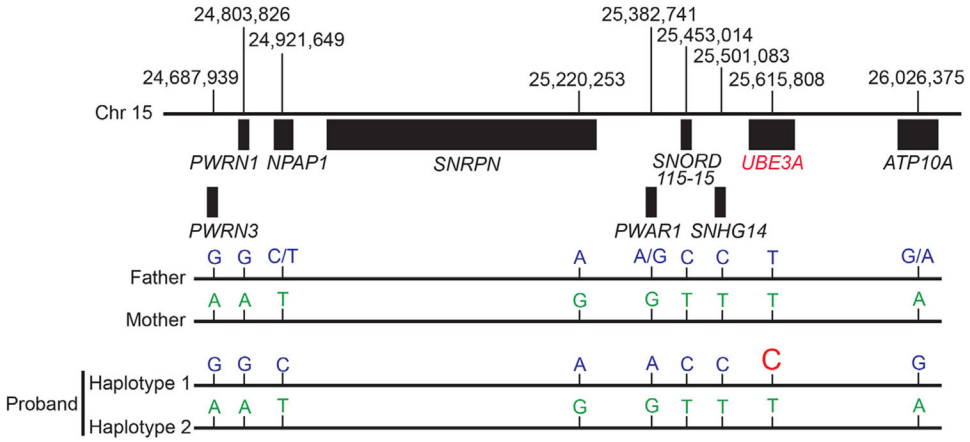

Figure 1.

Haplotype phasing the UBE3AT485A mutation in the autism proband SNPs on chromosome 15 near UBE3A identified from whole-exome sequence data of the parents and haplotype phased whole-genome sequence data from the autism proband (family ID: 13873). The T>C mutation resulting in UBE3AT485A co-segregates with the paternal haplotype in the autism proband. Genomic coordinates are based on hgGRCh37/hg19. Clinical data associated with this proband are available from the Simons Simplex Collection.

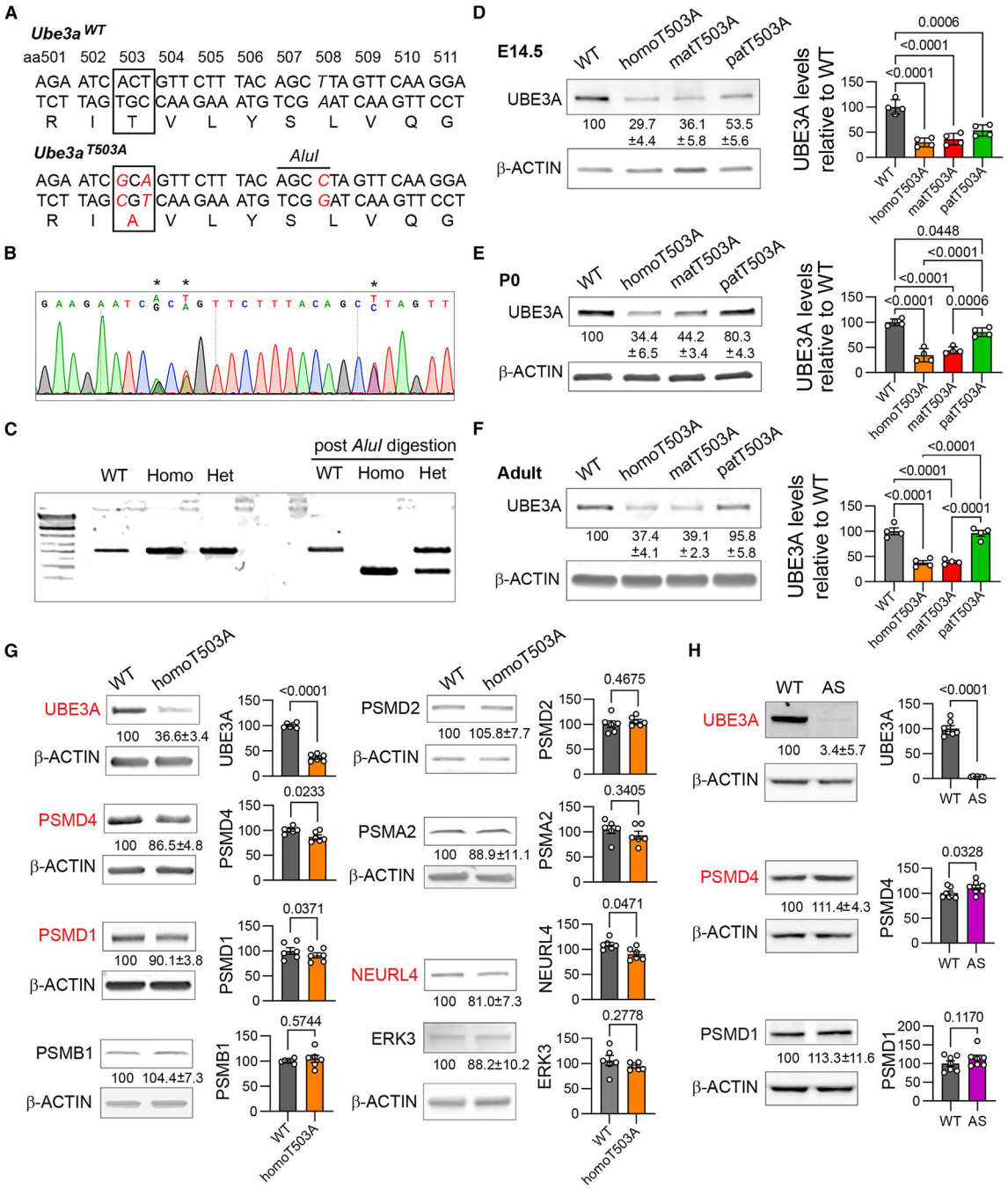

Figure 2. Generation of the *Ube3a*^{T503A} mouse model

(A) The ACT codon encoding T503 in mouse UBE3A (mouse NP_001380595.1, synonymous with human UBE3A^{T485A}) was mutagenized to GCA encoding alanine. A silent A>G point mutation was introduced to create an *AluI* restriction site to identify the *Ube3a*^{T503A} allele. aa, amino acid.

(B) Mutagenized nucleotides (asterisks) were detected by Sanger sequencing of PCR-amplified genome fragments from a heterozygous *Ube3a*^{T503A} mouse.

(C) Electrophoresis of DNA fragments amplified from WT and homozygous and heterozygous *Ube3a*^{T503A} mice by PCR before and after *AluI* digestion.
(D–F) UBE3A protein levels from the cerebral cortex of (D) E14.5, (E) P0, and (F) adult mutant and WT mice (n = 4).
(G) Western blot analyses of endogenous proteins that associate with UBE3A (n = 6).
(H) Western blot analyses of UBE3A, PSMD4, and PSMD1 from adult WT and AS model mice (n = 7).
For (D)–(H), protein levels were normalized to b-ACTIN. Levels of protein (mean ± SEM) relative to WT are shown below the representative blots. For (G)–(H), proteins with significant changes are in red.
See also Figures S1 and S2.

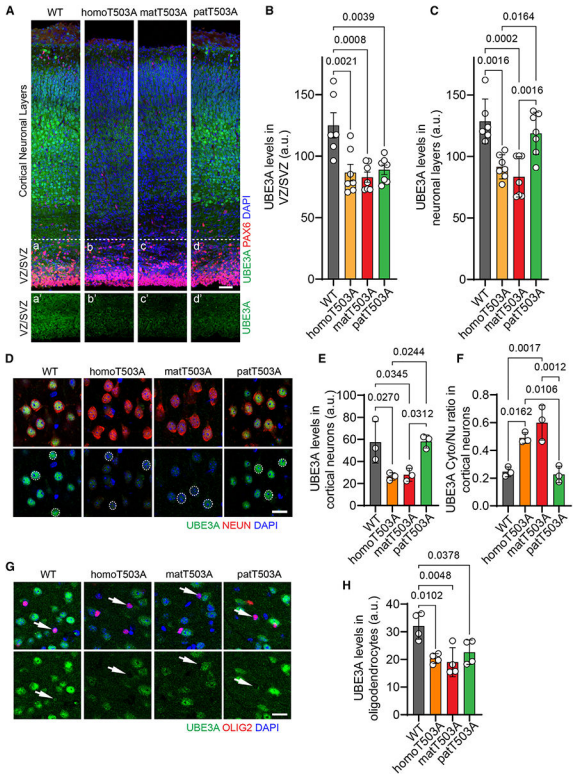

Figure 3. UBE3A protein levels in cortical neurons and progenitors of *Ube3a*^{T503A} mice

(A–C) Immunostaining of UBE3A in the P0 cerebral cortex (A). Progenitor cells in VZ/SVZ were co-labeled by PAX6 (a–d) and UBE3A (a′–d′). Quantification of UBE3A levels in (B) the cortical plate and (C) VZ/SVZ (WT, n = 6; homoT503A, matT503A and patT503A, n = 7).

(D–F) Immunostaining of UBE3A (green) in cortical neurons (NEUN, red) of adult brains (D). Examples of nuclear areas (DAPI, blue) were highlighted by dotted lines. (E) Reduced UBE3A protein levels and (F) altered cytoplasmic/nuclear distribution of UBE3A in cortical neurons of homoT503A and matT503A, but not patT503A, mice compared with controls (n = 3).

(G and H) Immunostaining of UBE3A in cortical oligodendrocytes (OLIG2^{+}, red) of adult brains (G). (H) Reduced UBE3A (green) levels in OLIG2^{+} cells in homoT503A, matT503A, and patT503A mutant mice compared with *WT* controls (n = 4). Examples of OLIG2^{+} cells are indicated by arrows. Data are represented as mean ± SEM.

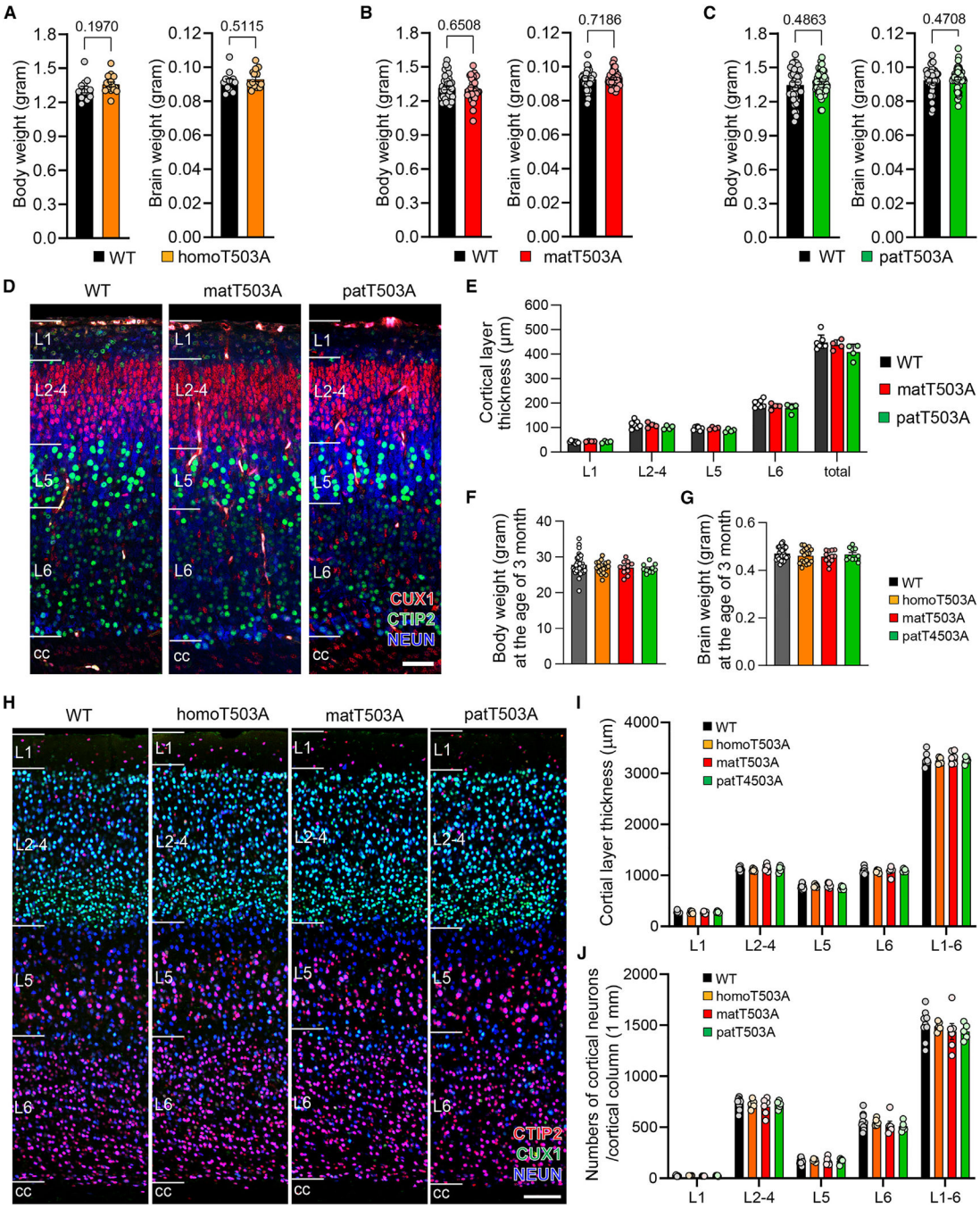

Figure 4. Cortical development is not grossly affected in *Ube3a*^{T503A} mutant mice

(A–C) Brain and body weight of homoT503A (WT, n = 12; homo, n = 15; from 4 litters) (A), matT503A (WT, n = 34; matT503A, n = 35; from 9 litters) (B), and patT503A (WT, n = 39; patT503A, n = 53; from 13 litters) (C) mice compared with WT mice at P0.

(D and E) Cortical thickness and lamination of P0 matT503A (D) and patT503A (E) mice (main effect of genotype, F (2, 12) = 2.466, p = 0.1267). Layers 2–4, CUX1^{+} in red; layers 5–6, CTIP2^{+} in green (WT, n = 7; matT503A and patT503A, n = 4).

(F and G) Body (main effect of genotype, $F(3, 71) = 0.7956$, $p = 0.5004$) (F) and brain weight (main effect of genotype, $F(3, 71) = 0.8223$, $p = 0.4859$) (G) of mice at 3 months (WT, n = 35; homoT503A, n = 18; matT503A, n = 12; patT503A, n = 10).
(H–J) Normal cortical lamination of adult homoT503A, matT503A, and patT503A mutant mice (H). (I) The thickness of cortical layers (main effect of genotype, $F(3, 21) = 0.4553$, $p = 0.7164$). (J) Neuronal numbers in each cortical layer (layer 1, $CTIP2^+$; layers 2–4, $CUX1^+$; layers 5 and 6, $CTIP2^+$) (main effect of genotype, $F(3, 21) = 0.4231$, $p = 0.7384$). Data are represented as mean ± SEM.

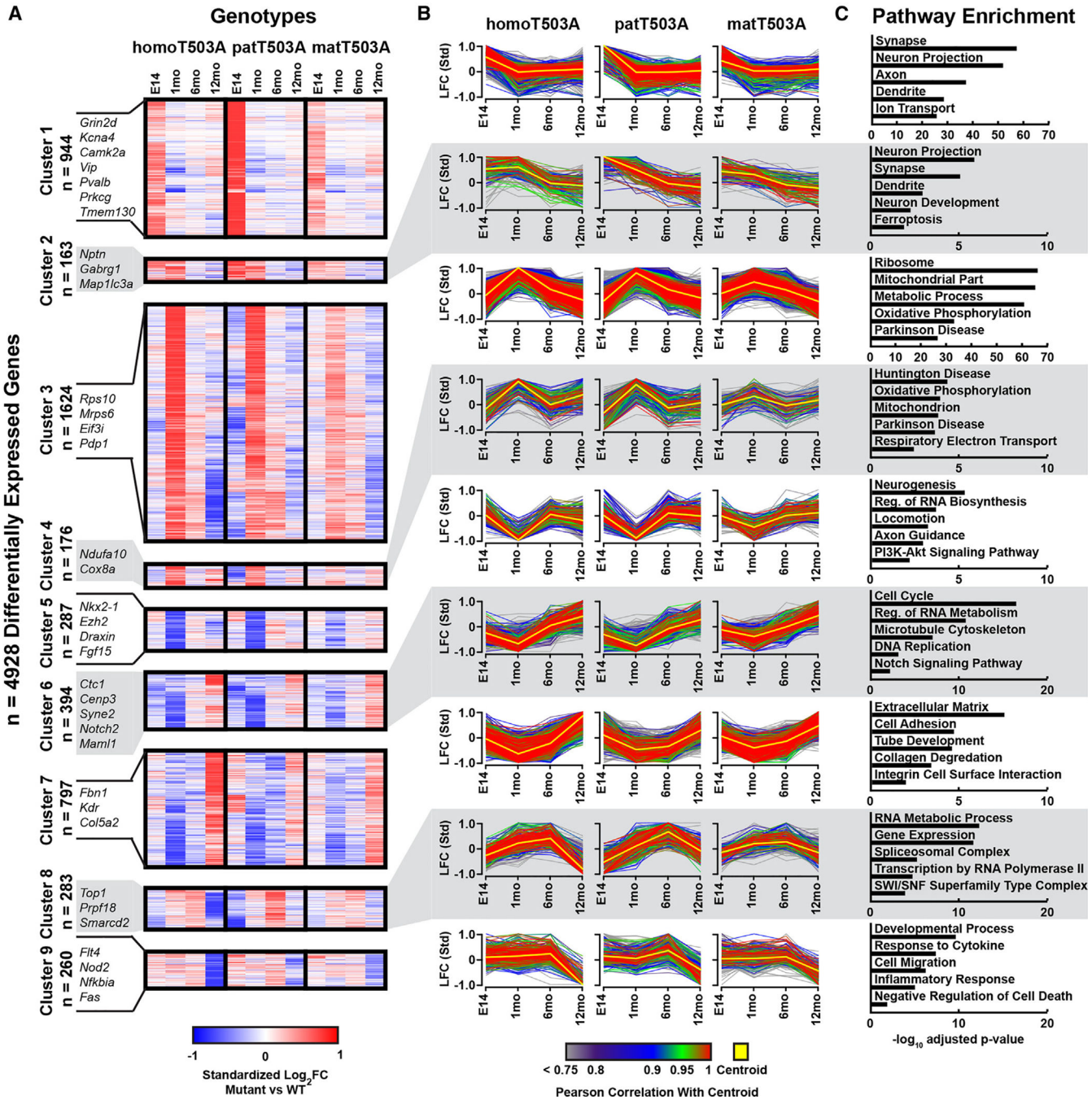

Figure 5. Differentially expressed genes in the cerebral cortex of *Ube3a*^{T503A} mutant mice across the lifespan

(A) Heatmaps summarizing DEGs in homoT503A, patT503A, and matT503A mice (standardized log2 fold change relative to WT control) at E14.5, 1 month,6 months, and 12 months of age. DEGs were categorized into nine clusters based on their temporal changes in transcript levels across all four ages. Examples of genes in each cluster are listed left of the heatmap graph. See also Figure S4.

(B) Averaged (centroid, in yellow) and individual trajectories of all differentially expressed genes in each group.

(C) GO analysis of DEGs.

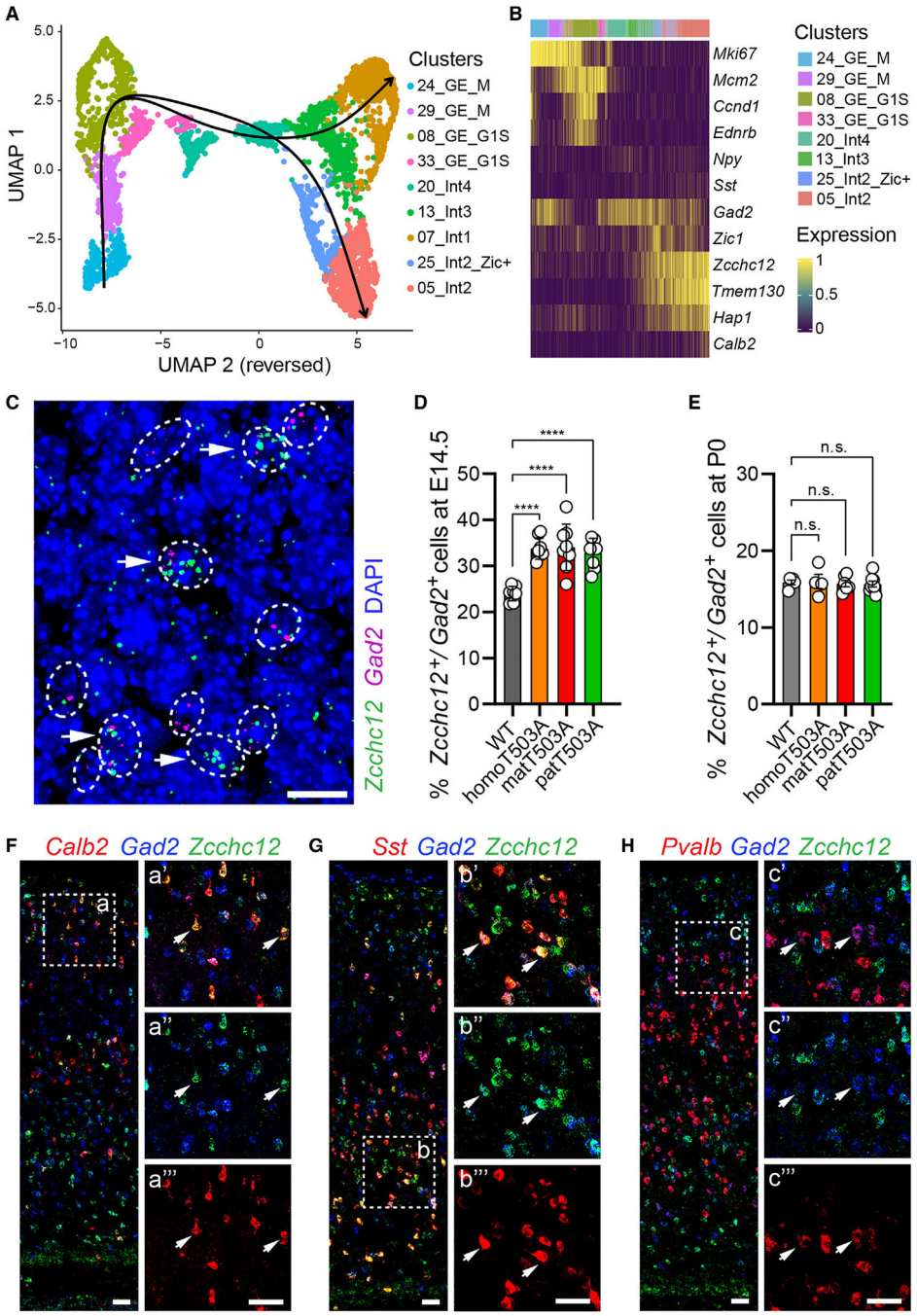

Figure 6. A cortical interneuron subclass is transiently expanded in embryonic *UBE3A*^{T503A} mutant mice

(A) Pseudotime analysis of interneurons (Int1, Int2, Int2_Zic^{+}, Int3, Int4) and progenitors in the GEs revealed two distinct interneuron developmental trajectories derived from GE progenitor cells. See also Figure S5.

(B) Unique gene expression signatures of Int2 and Int2_Zic^{+} interneurons among cells in lineage 1, ordered by pseudotime. Transcripts of *Zcchc12, Tmem130, Hap1, Peg1, Sst,* and *Calb2* are highly enriched in Int2 and Int2_Zic^{+} interneurons.

(C–E) Transient increase of Int2 interneurons validated by HCR single-molecule RNA hybridization. (C) A representative image showing HCR detection of *Gad2*$^{+}$ (magenta) and *Zcchc12*$^{+}$ (green) cells in the cortex at E14.5. *Gad2*$^{+}$ cells were highlighted by circles. *Gad2*$^{+}$ cells that express high levels of *Zcchc12* transcripts (R5 particles) counted as *Gad2*$^{+}$/*Zcchc12*$^{+}$ cells are indicated by arrows. Bar: 10 μm. (D) A transient increase of *Gad2*$^{+}$/*Zcchc12*$^{+}$ cells was observed in matT503A, patT503A, and homoT503A mice at E14.5 (one-way ANOVA, $F(3, 28) = 16.96$, $p < 0.0001$) (n = 8 for all genotypes). ****$p < 0.0001$. (E) Comparable proportions of *Gad2*$^{+}$/*Zcchc12*$^{+}$ cells between WT and mutant mice at P0 (one-way ANOVA, $F(3, 19) = 0.1053$, $p = 0.9560$) (WT, n = 5; homo, n = 4; matT503A, n = 6; matT503A, n = 8 animals). Data are represented as mean ± SEM.

(F–H) HCR detection of *Gad2*$^{+}$ (blue), *Zcchc12*$^{+}$ (green), and mature cortical interneuron markers (red), *Calb2* (F), *Sst* (G), or *Pvalb* (H).

Boxed areas (a), (b), and (c) were enlarged and are shown as (a′), (b′), and (c′) for triple labeling, (a″), (b″) and (c″) for *Zcchc12/Gad2* double labeling, and (a‴), (b‴), and (c‴) for interneuron subtype-specific markers. Examples of *Gad2*$^{+}$/*Zcchc12*$^{+}$ cells are indicated by arrows. Bar: 50 μm.

A

Summary of mouse bahavior tests

Behavioral Assay	homoT503A	matT503A	patT503A
Open field			
Total distance	**Increase**	**Increase**	N/C
Rearing	**Increase**	N/C	N/C
Center time	**Increase**	**Increase**	N/C
3-chamber			
Sociability	N/C	N/C	**Decrease**
Novelty preference	N/C	N/C	N/C
Entries	**Increase**	**Increase**	N/C
Rotarod	N/C	**Increase**	N/C
Elevated plus maze	N/C	N/C	N/C
Marble-bury assay	N/C	N/C	N/C
Olfactory test	N/C	N/C	N/C
Acoustic startle			
Amplitude	N/C	N/C	N/C
Prepulse inhibition	N/C	N/C	N/C
Hot plate	N/C	N/C	N/C

Bold, p<0.05 relative to WT;
N/C=no change (p>0.05 relative to WT).

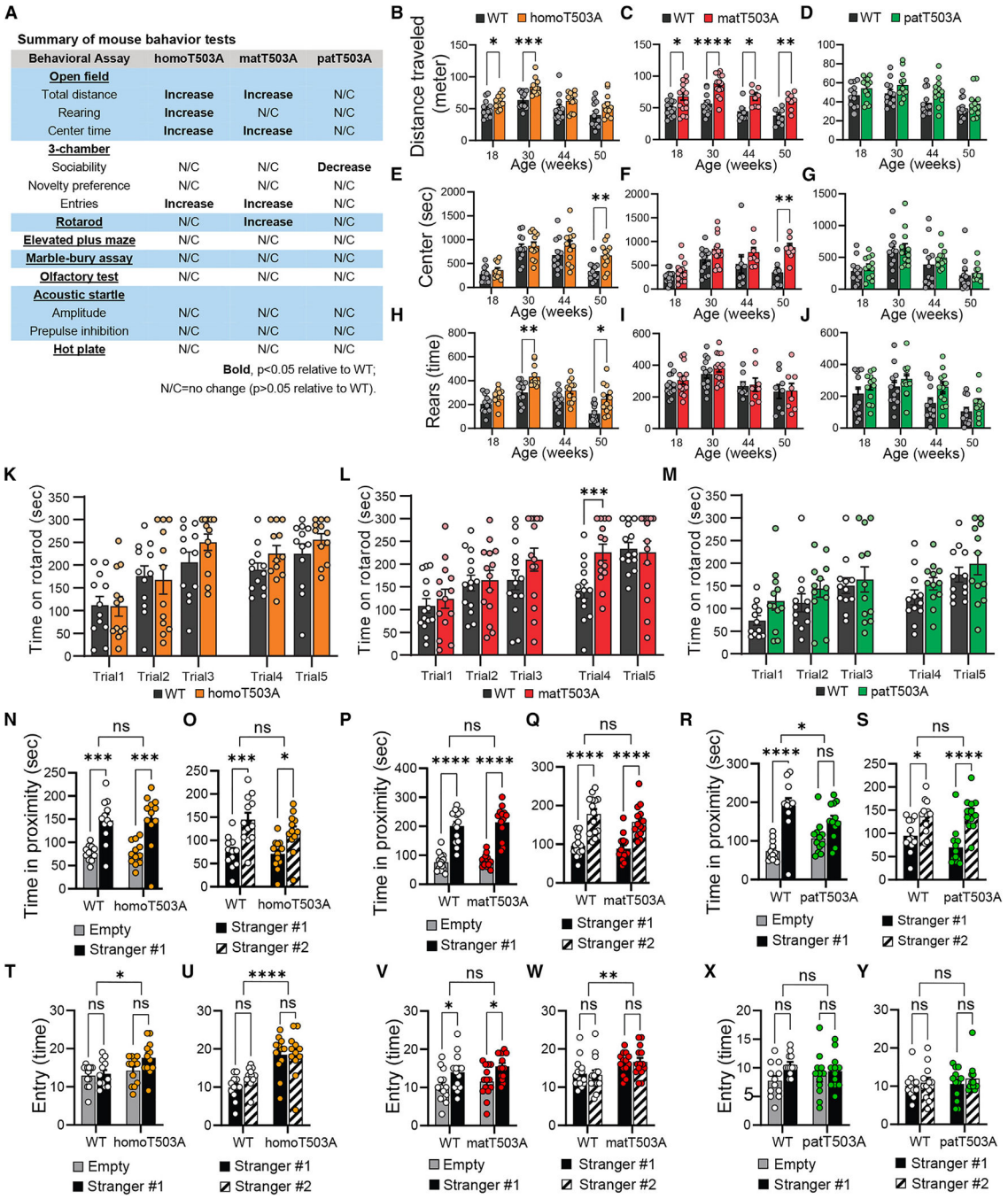

Figure 7. Behavioral phenotypes differ based on parent of origin of *Ube3a*^{T503A} allele and age

(A) Summary of mouse behavioral tests. homoT503A vs. WT, n = 12; matT503A vs. WT, n = 14 except open-field tests (n = 14 at 18 and 30–32 weeks, n = 8 at 43–44 and 50–52 weeks); patT503A vs. WT, n = 12.

(B–D) Total distance traveled as a function of age for (B) homoT503A (genotype × time interaction, F (3, 66) = 0.4913, p = 0.6895; main effect of genotype, F (1, 22) = 13.69, p = 0.0012); (C) matT503A (genotype × time interaction, F (3, 80) = 1.092, p = 0.3574; main effect of genotype, F (1, 80) = 47.17, p < 0.0001); and (D) patT503A (genotype × time

interaction, F (3, 66) = 0.5747, p = 0.6337; main effect of genotype, F (1, 22) = 3.636, p = 0.0697) mice and WT control.

(E–G) Time spent in the center as a function of age for (E) homoT503A (genotype × time interaction, F (3, 66) = 1.855, p = 0.1459; main effect of genotype, F (1, 22) = 4.919, p = 0.0372); (F) matT503A (genotype × time interaction, F (3, 54) = 2.033, p = 0.1202; main effect of genotype, F (1, 26) = 13.87, p = 0.001); and (G) patT503A (genotype × time interaction, F (3, 66) = 0.2716, p = 0.8457; main effect of genotype, F (1, 22) = 0.5475, p = 0.4671) mice and WT control.

(H–J) Rearing movements as a function of age for (H) homoT503A (genotype × time interaction, F (3, 66) = 1.102, p = 0.3546; main effect of genotype, F (1, 22) = 15.96, p = 0.0006); (I) matT503A (genotype × time interaction, F (3, 54) = 0.1444, p = 0.9328; main effect of genotype, F (1, 26) = 0.6869, p = 0.4148); and (J) patT503A (genotype × time interaction, F (3, 66) = 1.295, p = 0.2836; main effect of genotype, F (1, 22) = 2.659, p = 0.1172) mice and WT control.

(K–M) Rotarod tests of (K) homoT503A (genotype × trial interaction, F (4, 88) = 0.7928, p = 0.5330; main effect of genotype, F (1, 22) = 1.334, p = 0.2604; main effect of trial, F (4, 88) = 15.40, p < 0.0001); (L) matT503A (genotype × trial interaction, F (4, 104) = 2.232, p = 0.0.705; main effect of genotype, F (1, 26) = 2.592, p = 0.1195; main effect of trial, F (4, 104) = 11.56, p < 0.0001; ***p < 0.005, uncorrected Fisher's least significant difference [LSD] test); and (M) patT503A mice (genotype × trial interaction, F (4, 88) = 0.2453, p = 0.9118; main effect of genotype, F (1, 22) = 2.220, p = 0.1505; main effect of trial, F (4, 88) = 10, p < 0.0001). (N–S) Time spent in proximity. (N and O) HomoT503A and WT mice. (N) No difference between homoT503A and WT mice in sociability (genotype × side interaction, F (1, 22) = 0.07381, p = 0.7884) and (O) social novelty (genotype × side interaction, F (1, 22) = 2.231, p = 0.1495) tests. (P and Q) matT503A and WT mice. (P) No difference between matT503A and WT mice in sociability (genotype × side interaction, F (1, 26) = 0.1647, p = 0.6882) and (Q) social novelty (genotype × side interaction, F (1, 26) = 0.434, p = 0.5158) tests. (R and S) PatT503A and WT mice. (R) patT503A mice showed deficits in sociability test (genotype × side interaction, F (1, 22) = 7.462, p = 0.0122) but (S) normal social novelty tests (genotype × side interaction, F (1, 22) = 1.786, p = 0.1950). Unlike WT mice, which spend more time exploring the cage with stranger #1, patT503A mice did not show a preference for the social interactor over an empty cage.

(T–Y) Entry times as the measurement of three-chamber social behavior tests. (T) Significant differences were observed in homoT503A mice in both sociability (main effect of genotype, F (1, 44) = 6.826, p = 0.0122) and (U) social novelty tests (main effect of genotype, F (1, 44) = 32.98, p < 0.0001) compared with WT controls. (V) The entry times for matT503A mice were not different from WT controls in sociability tests (F (1, 52) = 1.733, p = 0.1938) but were significantly increased in (W) social novelty tests (F (1, 52) = 8.953, p = 0.0042) compared with WT controls. (X) The entry times of patT503A mice did not differ from WT controls in either the sociability test (main effect of genotype: F (1, 44) = 0.009679, p = 0.9221) or (Y) the social novelty test (main effect of genotype: F (1, 44) = 0.4528, p = 0.5045). Data are represented as mean ± SEM. *p < 0.05; **p < 0.01; ***p < 0.001, ****p < 0.0001.

See also Figure S6.

KEY RESOURCES TABLE

REAGENT or RESOURCE	SOURCE	IDENTIFIER
Antibodies		
mouse anti-UBE3A (3E5)	Sigma-Aldrich	Cat# SAB1404508; RRID:AB_10740376
rabbit anti-PSMD4	Cell Signaling	Cat# 3846; RRID:AB_2284381
rabbit anti-PSMD1	Atlas antibodies	Cat# HPA036736; RRID:AB_2675278
rabbit anti-PSMA2	Thermo Fisher Scientific	Cat# PA5–17294; RRID:AB_10987391
mouse anti-ERK3	Thermo Fisher Scientific	Cat# MA1–101; RRID:AB_2536749
rabbit anti-NEURL4	Thermo Fisher Scientific	Cat# PA5–63108; RRID:AB_2644633
rabbit anti-PSMB1	Thermo Fisher Scientific	Cat# PA5–49648; RRID:AB_2635102
rabbit anti-RAD23A	Proteintech	Cat# 51033–1-AP; RRID:AB_2253493
mouse anti-β-ACTIN	Sigma-Aldrich	Cat# A1978; RRID:AB_476692
rabbit anti-GFP	Novus	Cat# NB600–308; RRID:AB_10003058
mouse anti-Myc tag	Millipore	Cat# 05–724; RRID:AB_309938
guinea pig anti-NEUN	Millipore	Cat# ABN90P; RRID:AB_2341095
rabbit anti-CUX1	Santa Cruz	Cat# sc-13024; RRID:AB_2261231
rat anti-CTIP2	Abcam	Cat# ab18465; RRID:AB_2064130
rabbit anti-PAX6	BioLegend	Cat# 901301; RRID:AB_2565003
rabbit anti-OLIG2	Millipore	Cat# AB9610; RRID:AB_570666
donkey anti-rabbit IgG Alexa Fluor 568	Thermo Fisher Scientific	Cat# A10042; RRID:AB_2534017
goat anti-rat IgG Alexa Fluor 488	ThermoFisher Scientific	Cat# A-11006; RRID:AB_2534074
goat anti-mouse IgG2a Alexa Fluor 488	ThermoFisher Scientific	Cat# A-21131; RRID:AB_2535771
donkey anti-guinea pig IgG Alexa 647	Jackson ImmunoResearch	Cat# 706–605-148,; RRID:AB_2340476
IRDye 680RD-conjugated donkey anti-mouse polyclonal antibody	LI-COR Biosciences	Cat# 925–68072; RRID:AB_2814912
IRDye 800CW-conjugated donkey anti-rabbit	LI-COR Biosciences	Cat# 925–32213; RRID:AB_2715510
Critical commercial assays		
Dual-Luciferase reporter assay system	Promega	Cat# E1910
Experimental Models: cell lines		
HEK293T	ATCC	Cat# CRL-3216
Experimental models: Organisms/strains		
Ube3a^{T503A} mutant mice	this study	N/A
Ube3a knock-out mice	The Jackson Laboratory	Strain #:016590, RRID:IMSR_JAX:016590
Oligonucleotides		
Ube3aT503A-F	CCTCGAGTGGATCCACTAGAA	N/A
Ube3aT503A-R	ATTAGACAACCAGGATACCAGT	N/A

REAGENT or RESOURCE	SOURCE	IDENTIFIER
Recombinant DNA		
pCIG-UBE3A-WT-ires-EGFP	Yi et al., Cell, 2015	N/A
pCIG-UBE3A-T485A-ires-EGFP	Yi et al., Cell, 2015	N/A
pCIG-UBE3A-LD-ires-EGFP	Yi et al., Cell, 2015	N/A
pCIG-UBE3A-T787A-ires-EGFP	generated in this study	N/A
pCIG-UBE3A-T787A-LD-ires-EGFP	generated in this study	N/A
pCIG-UBE3A-T485A-LD-ires-EGFP	Yi et al., Cell, 2015	N/A
BAR-pGL3	Yi et al., JBC, 2017	N/A
pRL-TK-Renilla luciferase	Promega	N/A
Software and Algorithms		
ImageJ	https://imagej.net/	RRID:SCR_003070
GraphPad Prism	https://www.graphpad.com/	RRID:SCR_002798
Adobe Photoshop	Adobe	RRID:SCR_014199
FASTXtoolkit 0.0.14	http://hannonlab.cshl.edu/fastx_toolkit/index.html	RRID:SCR_005534
cutadapt 1.12	https://cutadapt.readthedocs.io/en/stable/	RRID:SCR_011841
Salmon 0.11.3	https://github.com/COMBINE-lab/Salmon	https://doi.org/10.1038/nmeth.4197
DESeq2 1.22.2	http://www.bioconductor.org/packages/release/bioc/html/DESeq2.html	RRID:SCR_015687
gprofiler2	https://biit.cs.ut.ee/gprofiler/page/r	RRID:SCR_018190
tximport	https://github.com/mikelove/tximport	RRID:SCR_016752
scTransform v1	https://github.com/satijalab/sctransform	RRID:SCR_022146
Slingshot	https://github.com/kstreet13/slingshot	RRID:SCR_017012
tradeSeq	https://github.com/statOmics/tradeSeq	RRID:SCR_019238
ComplexHeatmap	https://bioconductor.org/packages/release/bioc/html/ComplexHeatmap.html	RRID:SCR_017270
ggplot2	https://cran.r-project.org/web/packages/ggplot2/index.html	RRID:SCR_014601
R code used to analyze scRNA-seq data	https://github.com/jeremymsimon/Xing_Ube3a/tree/v1.0	https://doi.org/10.5281/zenodo.8007302